Final Report
Improving CAMx Performance in Simulating Ozone Transport from the Gulf of Mexico

Prepared for:
Texas Commission on Environmental Quality
121 Park 35 Circle MC 164
Austin, TX 78753

Prepared by:
Greg Yarwood, Jaegun Jung, Ou Nopmongcol and Chris Emery
ENVIRON International Corporation
773 San Marin Drive, Suite 2115
Novato, California, 94945
www.environcorp.com
P-415-899-0700
F-415-899-0707

September 2012

Project Number 0626408I

Work Order No. 582-11-10365-FY12-05

ENVIRON

CONTENTS

Tables

Figures

Executive Summary

The TCEQ uses the Comprehensive Air Quality Model with Extensions (CAMx) to perform photochemical ozone modeling for Texas' State Implementation Plan (SIP). CAMx must correctly represent the ozone content of air entering Texas (background ozone) in order to model correctly the total ozone content of air over Texas and the response of ozone to emission reductions in Texas. CAMx tends to over-predict by ~20 ppb the background ozone in marine air entering Texas from the Gulf of Mexico. This study evaluated three factors that could contribute to over-predicting ozone over the Gulf of Mexico: (1) Under-estimated dry deposition of ozone over water; (2) Over-estimated CAMx boundary conditions for ozone over the Gulf of Mexico and/or Atlantic Ocean, and (3) Chemical reactions of iodine that deplete ozone in the marine boundary layer and are not included in CAMx.

Two dry deposition schemes in CAMx (called the Wesely and Zhang schemes) were reviewed and their over-water predictions for ozone deposition compared to measured deposition velocities over the Gulf of Mexico, Atlantic Ocean and other oceans. The measured ozone deposition velocities have systematic dependencies on sea surface temperature and wind speed. The Wesely scheme in CAMx under predicted whereas the Zhang scheme generally over predicted the ozone deposition velocity over ocean waters. ENVIRON implemented in both algorithms a single modification that describes how the ozone deposition velocity depends upon sea surface temperature and wind speed. The modified Zhang scheme was tested using the TCEQ's Rider 8 CAMx dataset for June 2006. As expected, ozone concentrations over the Gulf and Atlantic generally increased by 5-15 ppb with the modified Zhang scheme since deposition velocities generally decreased relative to the original algorithm.

Ozone concentrations at the boundaries of TCEQ's CAMx domain are extracted from global simulations performed using the GEOS-Chem or MOZART4 models. Over 20 global models, including GEOS-Chem and MOZART4, were evaluated for their performance in simulating Gulf Coast ozone in studies for the Task Force on Hemispheric Transport of Air Pollution (HTAP) 2007 interim assessment. All models but one (the LMDZ-INCA model from France) over-predicted Gulf Coast ozone from June to September by ~20 ppb on average. The formulation of the LMDZ-INCA model is not substantially different from other models although the driving meteorology (ECMWF ERA-40 data) may partly explain why LMDz-INCA performed well.

Most global models, including GEOS-Chem and MOZART4, employ horizontal grid resolutions of several hundred km. The ability of GEOS-Chem and MOZART to distinguish marine air over the Gulf of Mexico from continental air was investigated by reviewing model output for June 2006. Both models show a concentration gradient from higher ozone over land to lower over the Gulf, but the gradient is spread over several grid cells (500 km or greater). Keep in mind that the Gulf is ringed by land with several US states to the north, Florida to the east, Cuba and the Yucatan peninsula to the south and Mexico to the west. Consequently, only near the center of the Gulf can GEOS-Chem and MOZART represent air as being marine in character and not influenced by land-based emissions. Coarse model resolution can explain why GEOS-Chem and MOZART over-predict summer ozone at Gulf Coast monitors. By extension, we expect that GEOS-Chem and

MOZART over-predict ozone at the boundaries of the TCEQ's CAMx grid. A sensitivity test with reduced ozone at the CAMx boundaries over the Gulf and the Atlantic showed that ozone high bias in GEOS-Chem can influence CAMx ozone at Gulf Coast monitors by 5 – 10 ppb.

Atmospheric reactions of iodine atoms deplete ozone catalytically, meaning that a single iodine atom can destroy many ozone molecules. Iodine compounds are emitted from ocean waters through biological and photochemical mechanisms and the oceans are the largest source of atmospheric iodine. Several field studies and numerous laboratory experiments have investigated how iodine depletes ozone and forms new aerosol particles in marine environments. ENVIRON developed a chemical mechanism for iodine and ozone and an emission model for oceanic emissions of iodine compounds for use with CAMx. The iodine-ozone mechanism was integrated with CB6 in CAMx and tested using the Rider 8 modeling database developed by TCEQ for June 2006. CAMx sensitivity tests indicate that iodine chemistry may cause up to about 5 ppb of ozone depletion over the Gulf of Mexico and at coastal monitors in Texas. These estimates are uncertain because emissions of iodine-containing compounds are uncertain and no measurements are available in Texas for model evaluation.

Detailed field study measurements for iodine and bromine at the Cape Verde Islands in the tropical Atlantic Ocean have shown that bromine reactions cause ozone depletion comparable to iodine, and that iodine and bromine act synergistically. Accordingly, we recommend extending the emissions and chemistry algorithms developed here for iodine to also include bromine. We also recommend that global models used to develop ozone boundary conditions for TCEQ's CAMx modeling also should include reactions and oceanic emissions for include bromine.

1.0 INTRODUCTION

The TCEQ uses the Comprehensive Air Quality Model with Extensions (CAMx) to perform photochemical ozone modeling for Texas' State Implementation Plan (SIP). CAMx must correctly represent the ozone content of air entering Texas (background ozone) in order to model correctly the total ozone content of air over Texas and the response of ozone to emission reductions in Texas. Back-trajectory analyses completed by the TCEQ suggest that air-masses influenced by passage over the North American continent contain background ozone levels that approach continental background ozone levels. In contrast, air masses with marine origins far out over the Gulf and the tropical Atlantic Ocean contain very little ozone, often below 20 parts per billion (ppb).

CAMx tends to over-predict by ~20 ppb the background ozone in marine air entering Texas from the Gulf of Mexico as illustrated by Figure 1-1 which shows hourly ozone monitored at Galveston airport and simulated for the TCEQ's Rider 8 modeling of June 2006. Figure 1-2 shows the location of Galveston Airport adjacent to the Gulf of Mexico and that this monitor site is well placed to measure the amount of ozone in background air from the Gulf of Mexico. The observed hourly ozone at Galveston Airport in June 2006 varied from less than 15 ppb (on June 2, 13 and 19) to over 100 ppb (on June 9) and back-trajectory analysis (Figure 1-3) indicates that this wide range results from transitions between periods of marine and continental influence. CAMx over-predicts ozone at Galveston Airport throughout June 2006. Over-prediction of ozone in marine air from the Gulf of Mexico can be clearly identified by focusing on the period from June 16-18, 2006, when back-trajectory analysis (Figure 1-3) shows that on-shore winds prevailed. CAMx has less tendency to over predict ozone at Galveston on days with clear continental influence such as June 27, 2007 (Figure 1-4).

Factors that could contribute to over-predicting ozone over the Gulf of Mexico include under-estimated dry deposition of ozone over water, over-estimated CAMx boundary conditions for ozone over the Gulf/Atlantic resulting from positive ozone bias in global models, and missing chemical reactions that deplete ozone in the marine boundary layer. Data are available to investigate each of these potential factors as discussed in Sections 2-4 of this report. Briefly, ozone deposition velocities over the Gulf were measured during TexAQS II (Helmig et al., 2012) and may be used to evaluate CAMx deposition velocities in Section 2. An inter-comparison of 20 global models (including GEOS-Chem) for the Task Force on Hemispheric Transport of Air Pollution (Fiore et al., 2009) found that most (but not all) models tended to over-predict summer ozone in a region of the southeastern United States (US) that included portions of the Gulf Coast as discussed in Section 3. Atmospheric reactions of iodine atoms, produced by photolysis of iodine compounds emitted from the ocean, are known to deplete ozone in marine environments (Chameides and Davis, 1980; Sommariva et al., 2012) as discussed in Section 4. Conclusions and recommendations are presented at the end of report sections 2-4.

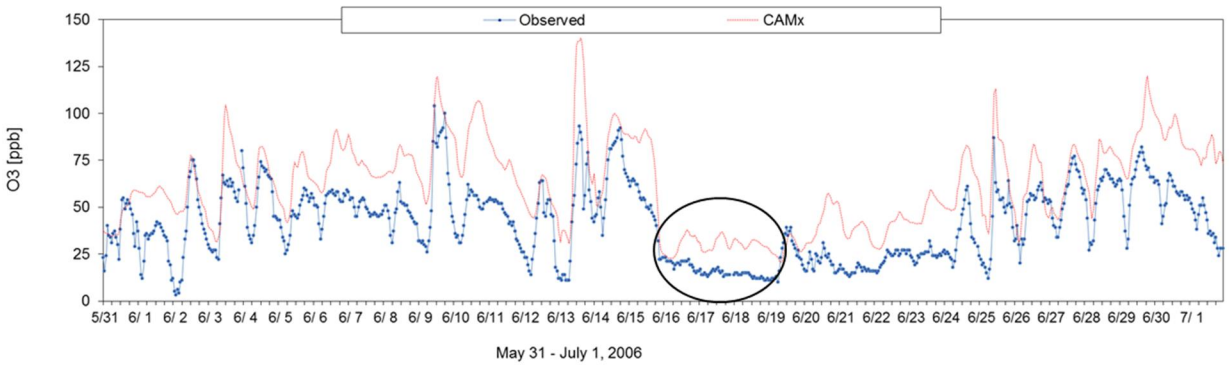

Figure 1-1. Hourly ozone (ppb) at the Galveston airport monitor for the TCEQ's Rider 8 modeling of June 2006. On-shore winds with less than 20 ppb ozone prevailed from June 16-18, 2006.

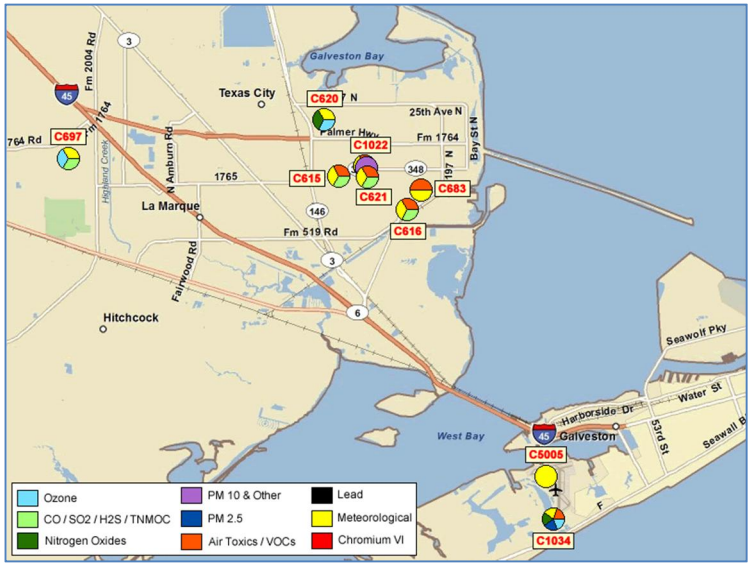

Figure 1-2. Location of the TCEQ's Galveston airport ozone monitor (C1034) adjacent to the Gulf of Mexico (map courtesy of TCEQ).

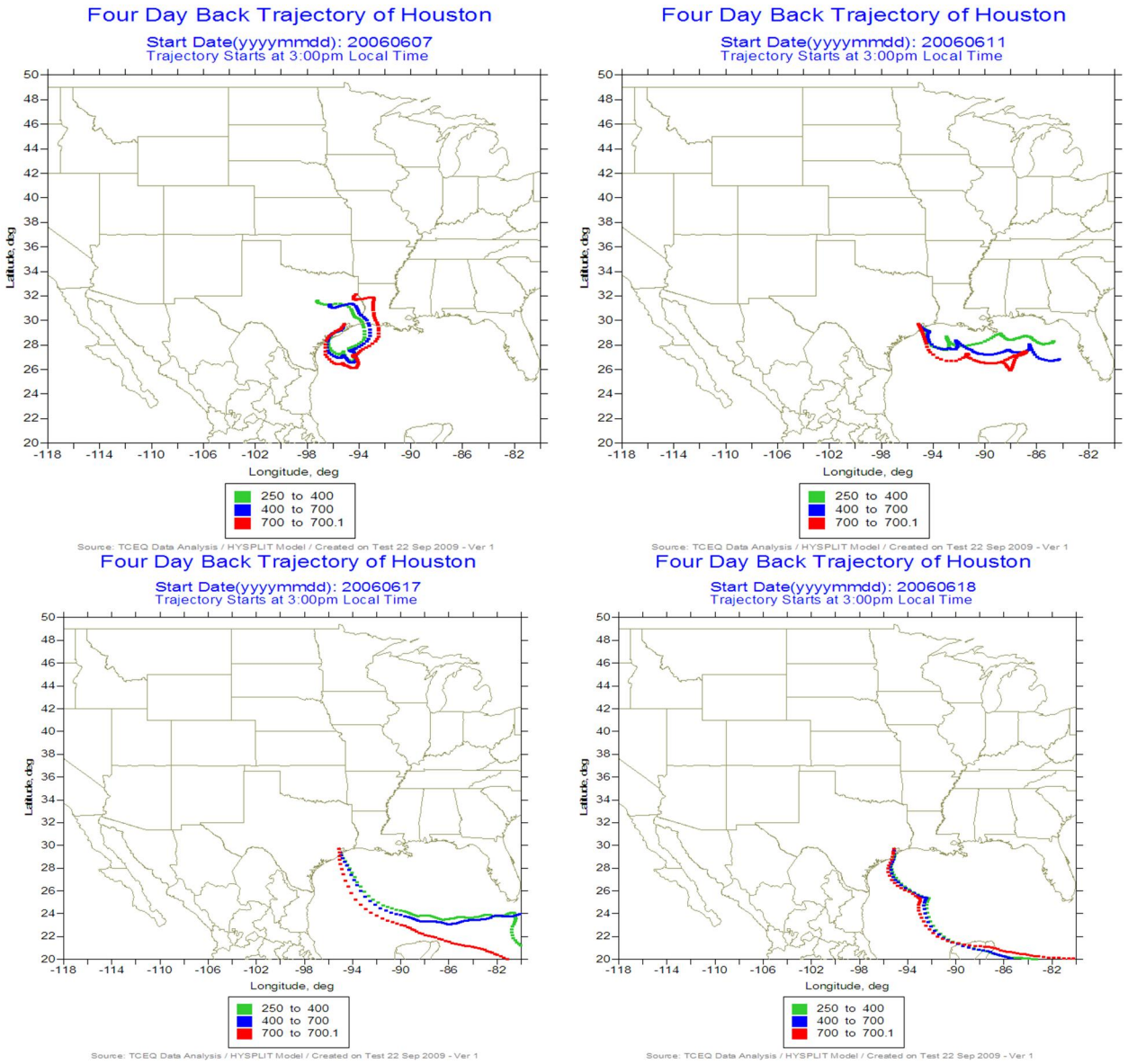

Figure 1-3. Back trajectories for Houston at 3 pm on several dates in June 2006 with on-shore flow from the Gulf of Mexico. Colors denote ending altitude (m). Figures courtesy of TCEQ.

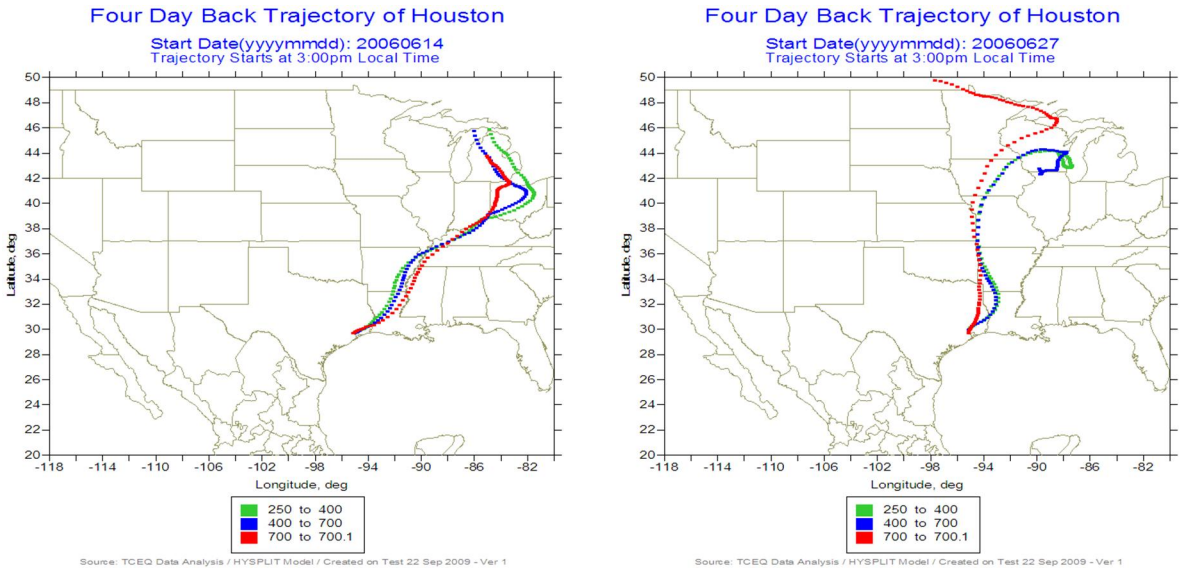

Figure 1-4. Back trajectories for Houston at 3 pm on two dates in June 2006 with continental airflow. Colors denote ending altitude (m). Figures courtesy of TCEQ.

2.0 EVALUATE CAMX OZONE DEPOSITION VELOCITIES

Deposition to the Earth's surface can be a significant loss process for many airborne pollutants. While "wet" deposition in rain can be significant for soluble gas species, it operates over limited spatial and temporal scales. "Dry" deposition operates constantly and is regulated by the chemical properties of a given gas (solubility, diffusivity, reactivity), the weather, the surface type, and for some surfaces, the time of day (e.g., uptake into photo-sensitive biota). Ozone has unique characteristics that influence its dry deposition. It is only moderately soluble, so its diffusion into water-containing surfaces is slow; however, it is highly reactive and so the net ozone flux from air to surface is driven more by its chemical reaction upon contact with a surface.

2.1 Deposition Models

Chemical transport models like CAMx employ a first-order flux calculation, driven by a "deposition velocity" (V_d), to simulate the transfer rate of an airborne gas at concentration C to the surface:

$$F = V_d C$$

This flux is often used as the surface boundary condition for the vertical diffusion term of the transport equation. Most models calculate V_d through the use of a resistance equation analogous to an electric circuit:

$$V_d = \frac{1}{R_a + R_b + R_s}$$

The first resistance in series (R_a) represents the ability of the surface boundary layer (~10-50 m depth) to turbulently transfer the gas to the surface. It is high during calm, stable conditions that resist vertical transfer, and minimum during windy and/or unstable conditions that create turbulent transport. The second resistance (R_b) represents the ability of a gas to diffuse through the thin laminar air layer (few millimeters) just above a surface element. It is high for gasses with low diffusivities, and vice versa. These first two resistances are generally well-characterized according to weather conditions and the known properties of gasses.

The third resistance (R_s) represents the ability of a gas to be taken up by contact with the surface either through absorption, dissolution, and/or reaction. This resistance depends on a multitude of factors, including the surface type (e.g., water, soil, concrete, organic litter, or plant stomatal and mesophyll openings), the surface condition (e.g., wetness, temperature, sun exposure) and the properties of the gas (e.g., solubility, diffusivity, reactivity). It is this resistance term that varies most among different deposition models.

For this report we focus on dry deposition of ozone to ocean surfaces. There are two dry deposition schemes available in CAMx:

1. The original Wesely (1989) algorithm, in which the R_s term has been modified for water surfaces following Sehmel (1980):

$$R_s = \frac{1}{3.9\times10^{-5} H T_s u^*}$$

   where H is the temperature-dependent Henry's Law constant, T_s is surface temperature in Kelvin, and u^* is turbulent wind stress or "friction velocity" (proportional to wind speed).

2. The newer Zhang (2003) algorithm, in which the R_s term over water is set to a constant value of about 2000 s/m (setting an upper limit on ozone V_d at 0.05 cm/s).

Both schemes possess very similar equations for R_a and R_b, so we will ignore their minor differences. Note that the Sehmel resistance equation is inversely proportional to gas solubility, sea surface temperature, and wind stress. Ozone solubility decreases with increasing temperature, which increases resistance and reduces deposition velocity. This effect is countered to a minor degree by increasing sea surface temperature and increasing wind stress, which both decreases resistance and increases deposition velocity.

2.2 Ship-born Ozone Deposition Velocity Measurements

Helmig et al. (2012) report results from eddy covariance ozone flux measurements taken aboard NOAA's *RV Ronald Brown* on five cruises during 2006-2008. These experiments provide the first ship-borne open-ocean ozone flux measurements. The cruises spanned a variety of sea states, weather conditions, and surface temperatures. One cruise in 2006 occurred in the Gulf of Mexico off the Texas coastline during the TexAQS II field monitoring campaign. Other cruises included the 2006 STRATUS off the coast of Chile, the 2007 GOMECC in the Gulf of Mexico and along the US Atlantic seaboard, the 2008 GasEx in the Southern Ocean east of Argentina, and the 2008 AMMA from Brazil north to the Caribbean (refer to the paper for a description of each). A combined ~1700 hours of 10-minute flux data were collected and analyzed to analyze medians and variability of ozone deposition velocity.

The median ozone deposition velocity among all five cruises ranged from 0.009 to 0.034 cm/s. During the TexAQS cruise, the median was 0.034 with a range of 0.009 to 0.065 cm/s, by far the largest deposition fluxes measured among all cruises. Helmig et al. state that the range of measurements from all five cruises is at the low end of previously reported data in the literature (0.01 to 0.12 cm/s). As we illustrate below, measurement data show that deposition velocities are positively correlated with wind speed and possibly with temperature. However, their comparison of measurement data to current global modeling algorithms of oceanic ozone uptake suggest that the temperature sensitivity may be an indirect reflection of biogeochemical conditions within the ocean's mixed layer, such as ozone reactions with aqueous iodide and unsaturated organic compounds.

We compared the range of observed ozone deposition velocities to predictions from both CAMx deposition modules, particularly focusing on the relationship to wind speed and surface temperature. Both the Wesely/Sehmel and Zhang algorithms were run outside of CAMx in a

separate testbed driver program that specified neutral stability conditions over the range of wind speeds and sea surface temperatures reported by Helmig et al. As in CAMx, the testbed determined sea surface roughness as a function of wind speed, which further influenced the R_a and R_b terms (and the R_s term in Wesely/Sehmel) through the wind stress variable u^*.

Figure 2-1 shows the comparison of measured and predicted ozone deposition velocities as a function of wind speed. In this case, the Wesely/Sehmel and Zhang predictions used a sea surface temperature of 30°C, consistent with the average temperature recorded during the TexAQS cruise. Interestingly, the degree to which measured deposition varies with wind speed appears to be related to surface temperature, with the TexAQS data (warmest) showing the largest wind speed dependence, and the STRATUS and GasEx data (coldest) showing no obvious wind speed dependence. The AMMA and GOMECC data (mildly warm temperatures) lie between the two extremes. The Zhang model predictions agree fairly well with the TexAQS data, but are generally over predicted. Recall that the Zhang R_s is set to a constant value, so the variability with wind speed, particularly below ~5 m/s, is related to changes in R_a. The Wesely/Sehmel model predictions are far below the TexAQS data by an order of magnitude.

Figure 2-2 shows a similar comparison as function of temperature. Here the separation of cruise data by temperature is clear. The Helmig et al. data plotted in Figure 2-2 is taken directly from their paper, and they state that wind speed effects were filtered out of the data (it remains unclear to us how this was done or how this effects the plotted data). To remain as consistent as possible, we ran the deposition algorithms with a constant 5 m/s wind speed and varied only the sea surface temperature (yet maintaining a neutral surface boundary layer). Again, the coldest data tend to be associated with the lowest deposition rates, while the warmest cruises

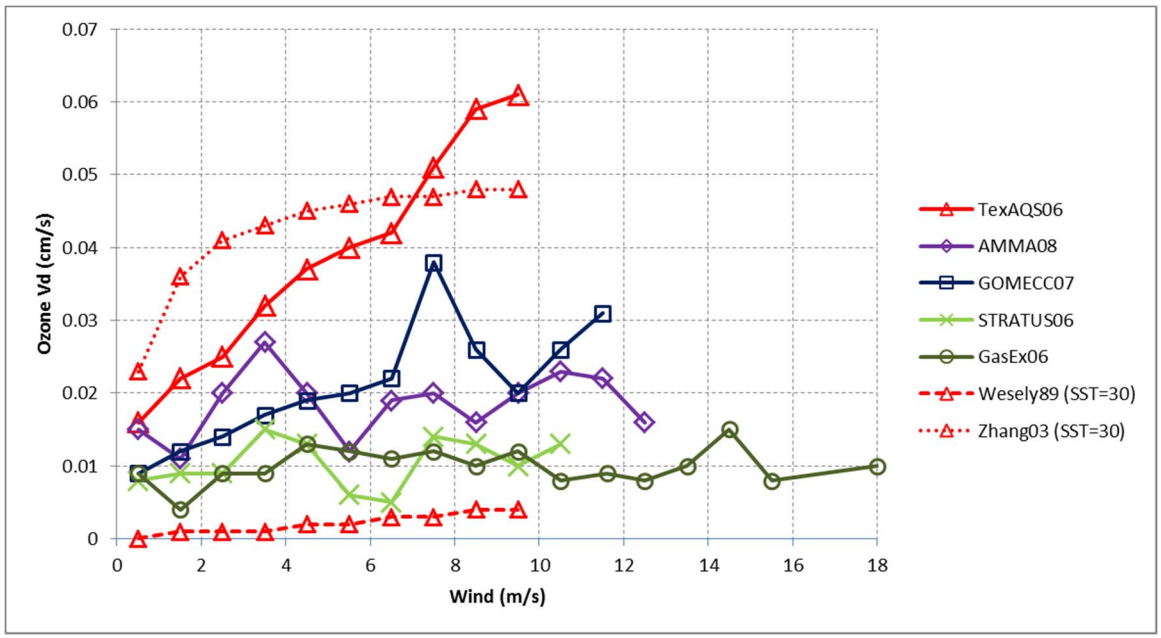

Figure 2-1. Measured (solid) and simulated (dotted/dashed) ozone deposition velocity (cm/s) as a function of wind speed (m/s). Measurements are taken directly from Figure 5 of Helmig et al. (2012), and they are color-coded by each of the five *RV Ronald Brown* cruises. The modeled data are from the CAMx Wesely/Sehmel and Zhang algorithms at a sea surface temperature of 30°C, consistent with the TexAQS cruise (i.e., compare red measurements with red predictions).

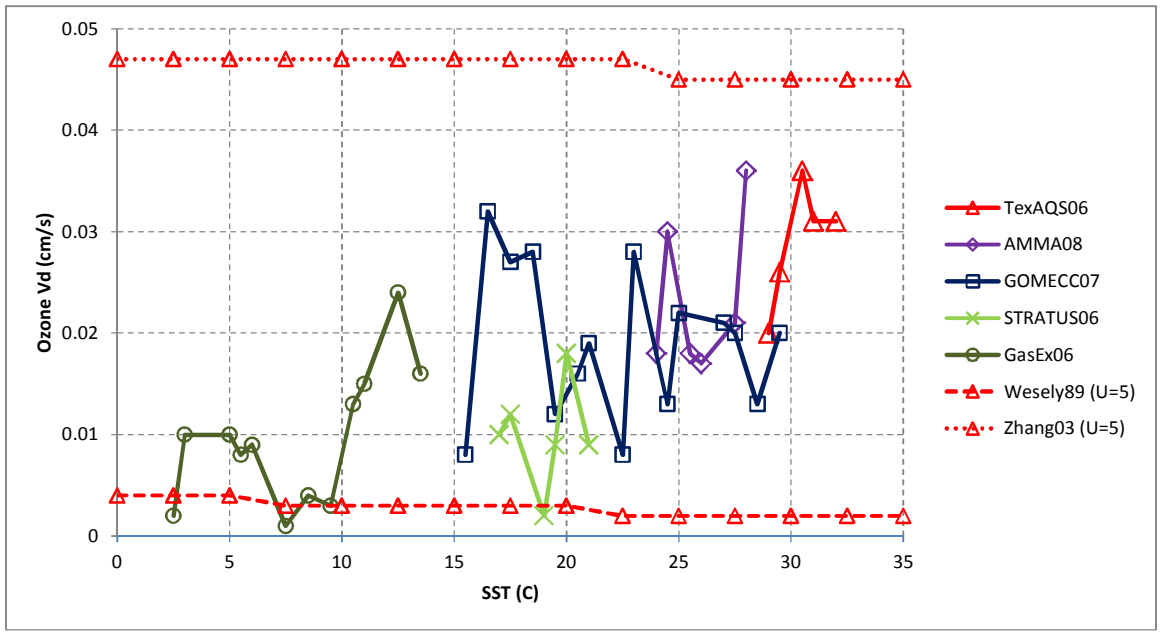

Figure 2-2. Measured (solid) and simulated (dotted/dashed) ozone deposition velocity (cm/s) as a function of surface temperature (°C). Measurements are taken directly from Figure 6 of Helmig et al. (2012), and they are color-coded consistently with Figure 2. The modeled data are from the CAMx Wesely/Sehmel and Zhang algorithms at a wind speed of 5 m/s.

are associated with the highest deposition rates. The Zhang model maintains a relatively constant deposition velocity just under 0.05 cm/s, as expected given constant R_s. The Wesely/Sehmel model is far under predicted and shows a weak reduction of deposition velocity with temperature because of the inverse dependence of the Henry's Law constant on temperature. This inverse temperature dependence was also noted by Helmig et al. when they compared their data to certain global model deposition predictions that included only solubility effects. Helmig et al. were able to obtain better matches when they included the effects of ozone reactions with iodine and organic matter (Ganzeveld et al., 2009). The particularly high ozone deposition rates measured over the warm Gulf of Mexico may be related to the high availability of chlorophyll, and potentially other dissolved organic matter, due to river discharges all along the coastline.

2.3 Modifications to CAMx Deposition Algorithms

To investigate the sensitivity of ozone predictions over the Gulf of Mexico to deposition velocity, we modified the Wesely and Zhang algorithms to parametrically match the tendencies of the measured data better. The Sehmel R_s equation for water surfaces was modified to use the following formula specific to ozone:

$$R_s^{O3} = \frac{1}{1\times10^{-4} + 5\times10^{-6} H\, u^* T_s^3}$$

where now T_s is in °C rather than Kelvin. The cubic temperature dependence overcomes the inverse temperature dependence of H and fits the deposition velocity response to the range of sea surface temperatures reported in the Helmig et al. data. The additional 1×10^{-4} term sets an upper limit on R_s and a lower limit on deposition velocity so that the latter does not fall much below 0.01 cm/s. This same equation replaced the constant R_s in the Zhang algorithm. For both Wesely and Zhang, a lower limit of 1500 s/m was placed on R_s such that ozone deposition over water does not exceed 0.065 m/s, which is the upper limit in the cruise data.

Figure 2-3 andFigure 2-4 are similar to Figure 2-1 andFigure 2-2, but show the new deposition velocity predictions resulting from the revised surface resistance equation. Figure 2-3 shows model predictions as a function of wind speed for three representative temperatures that correspond to the sea surface temperature ranges measured during TexAQS (30°C), AMMA/GOMECC (20°C), and STRATUS/GasEx (5°C). The revised algorithm adequately represents all measured data over the range of wind speed. Figure 2-4 shows the relationship with temperature for three wind speeds: 1, 5, and 10 m/s (recall that 5 m/s was assumed representative of the wind-filtered data of Helmig et al.). While the predictions for 5 m/s wind speeds adequately represent the means of the cruise data as a function of temperature, the 1 and 10 m/s predictions envelope most of the data nicely.

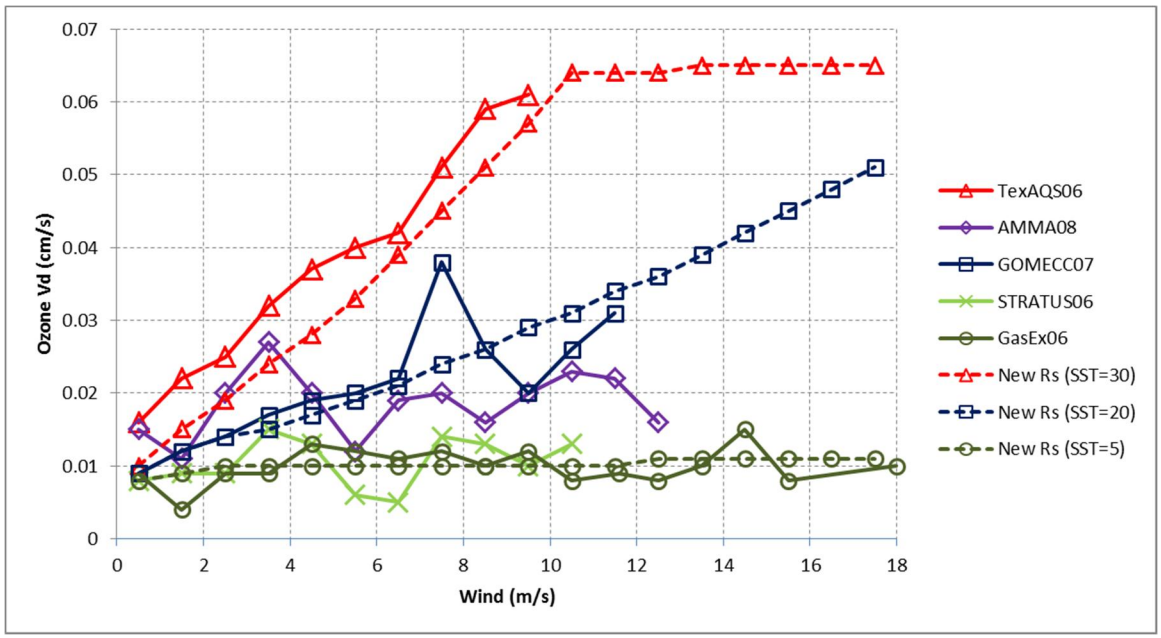

Figure 2-3. As in Figure 2-1, but with a revised surface resistance equation used in both Wesely/Sehmel and Zhang dry deposition models. The modeled data are given for three sea surface temperatures (5, 20, and 30°C).

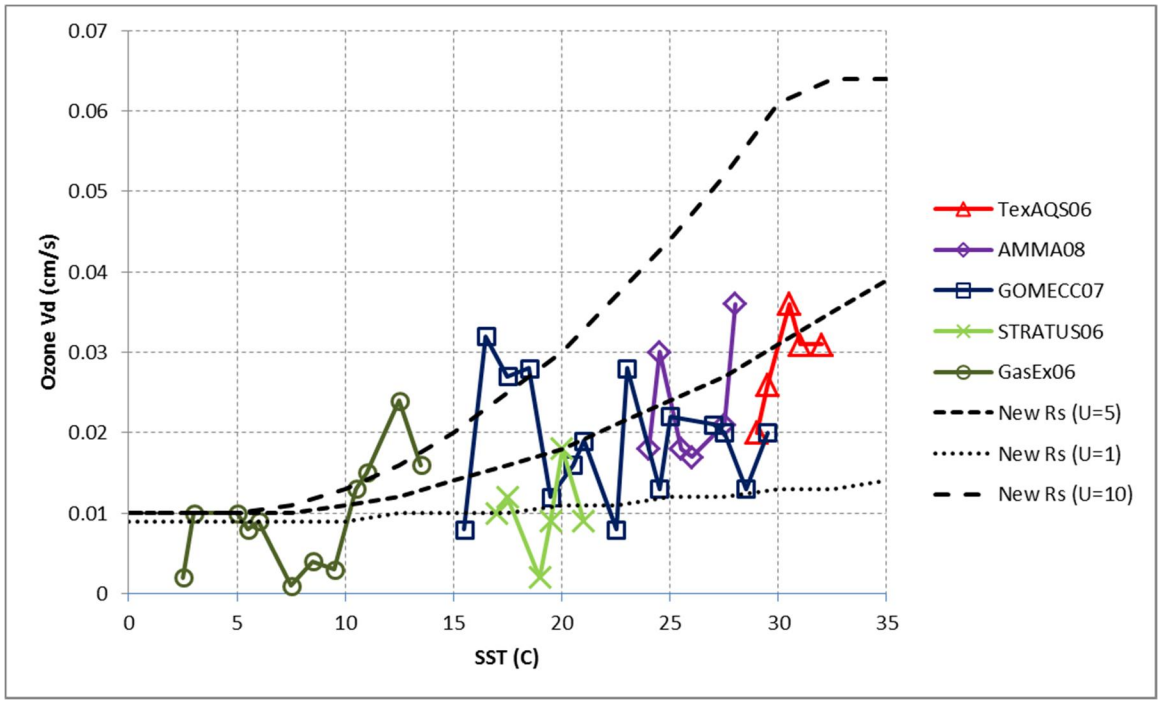

Figure 2-4. As in Figure 2-2, but with a revised surface resistance equation used in both Wesely/Sehmel and Zhang dry deposition models. The modeled data are given for three wind speeds (1, 5, and 10 m/s).

2.4 Results

Two CAMx runs were performed to evaluate ozone sensitivity to the deposition velocity change described above. Both runs used inputs developed by TCEQ for the Rider 8 May 31 – July 1, 2006 episode. TCEQ developed meteorology using WRF with the YSU PBL scheme, and configured CAMx version 5.40 to use the Zhang dry deposition scheme. We did not alter any of the TCEQ-derived model input datasets, but we did turn off the CAMx Plume-in-Grid (PiG) treatment for this analysis. The CAMx "BASE" run described below represents the standard TCEQ run without PiG. Our "DEPMOD" run used the modified over-water surface resistance for ozone in the Zhang dry deposition algorithm.

Figure 2-5 shows the difference in hourly ozone on the 36 km grid between the DEPMOD and BASE runs, specifically at two different hours when the maximum ozone differences occurred in the Atlantic and in the Gulf of Mexico. The maximum ozone differences occurred at times when ozone formed over land was being transported over water and removed by dry deposition to water. The modified Zhang dry deposition scheme increased ozone over water because the modification tended to reduce the ozone deposition velocity (demonstrated above in Figure 2-1 through Figure 2-4). The largest ozone increase is 14 ppb off the New York coast, whereas the largest increase in the Gulf is 7 ppb off the Texas coast.

Figure 2-6 presents the maximum and minimum hourly ozone difference over the entire simulation period. The top panel shows the maximum hourly ozone difference in each grid cell at any time during the simulation, while the bottom panel shows the minimum hourly difference. Again, these plots show that the tendency in the DEPMOD run is for higher ozone over the water bodies by 5-15 ppb (much lower ozone deposition), and these differences extend inland but dissipate rapidly. The minimum differences show some negative ozone impacts (slightly higher deposition) over the Gulf near Florida, but they do not exceed -0.3 ppb.

We did not perform CAMx sensitivity tests using the Wesely scheme because the Zhang scheme is the preferred option in CAMx. The sensitivity tests shown above (Figure 2-1 andFigure 2-2) showed poorer agreement between the Wesely scheme and the measured over-water deposition velocities than for the Zhang scheme. However, because the ozone surface resistance modification increases ozone deposition to water with the Wesely scheme, it is expected that the modification will reduce ozone concentrations. This modification will cause ozone deposition predicted the Zhang and Wesely schemes to converge over water.

2.5 Conclusion

Two dry deposition schemes in CAMx (called the Wesely and Zhang schemes) were reviewed and their over-water predictions for ozone deposition compared to measured deposition velocities over the Gulf of Mexico, Atlantic Ocean and other oceans (Helmig et al., 2012). The measured ozone deposition velocities have systematic dependencies on sea surface temperature and wind speed. The Wesely scheme in CAMx under predicted whereas the Zhang scheme generally over predicted the ozone deposition velocity over ocean waters. ENVIRON implemented in both algorithms a single modification that describes how the ozone deposition

velocity depends upon sea surface temperature and wind speed. The modified Zhang scheme was tested using the TCEQ's Rider 8 CAMx dataset for June 2006. As expected, ozone concentrations over the Gulf and Atlantic generally increased by 5-15 ppb with the modified Zhang scheme since deposition velocities generally decreased relative to the original algorithm.

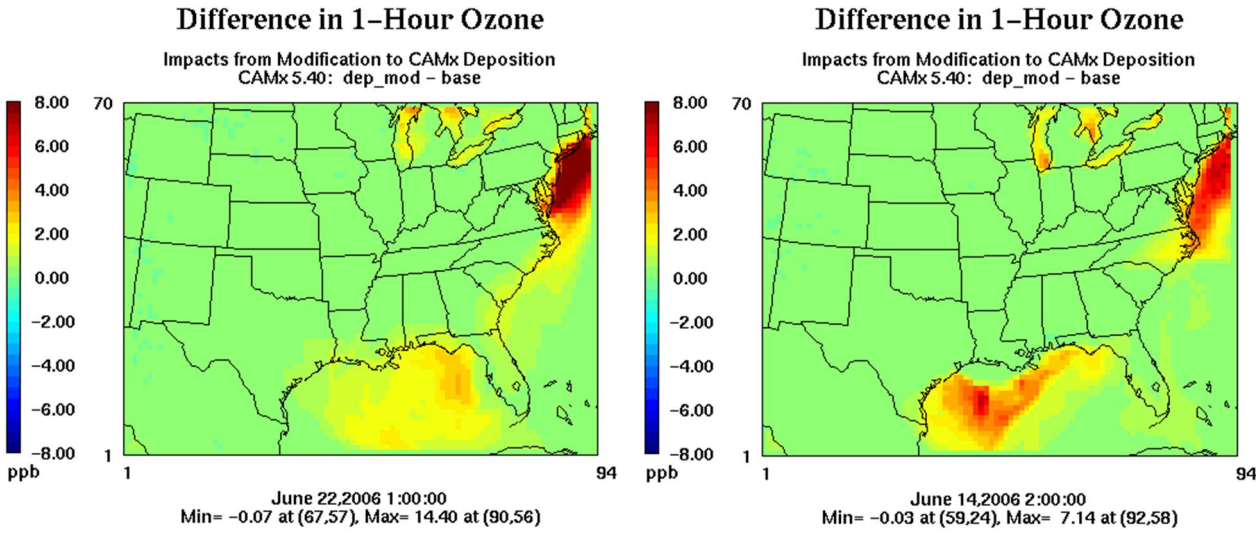

Figure 2-5. Difference in hourly ozone on the 36 km CAMx modeling grid between the DEPMOD and BASE simulations of June 2006. (Left) time of maximum difference occurring over the Atlantic Ocean; (right) time of maximum difference occurring over the Gulf of Mexico.

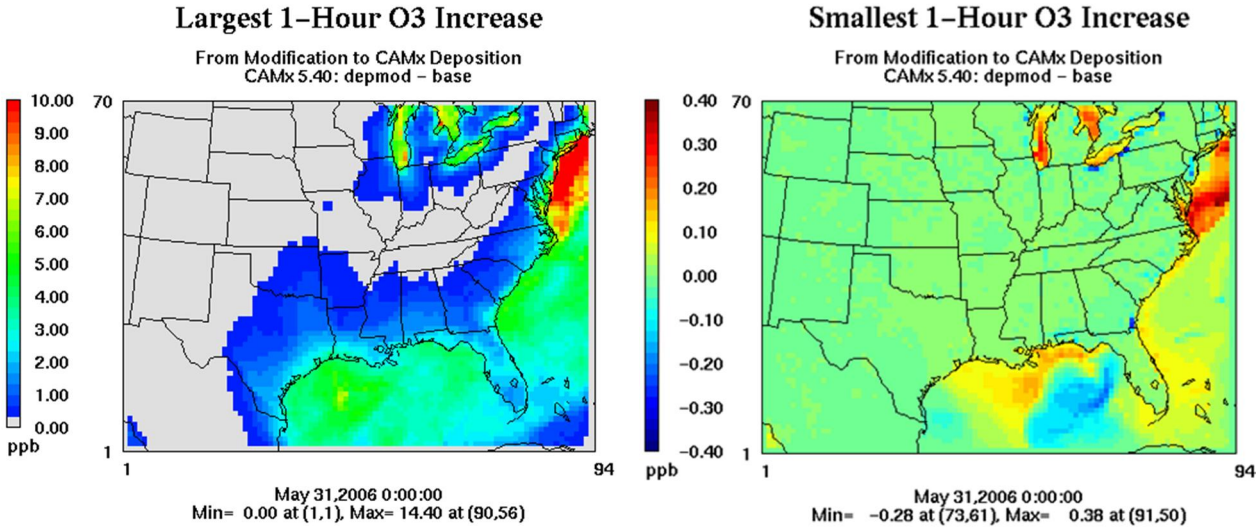

Figure 2-6. Maximum (left) and minimum (right) ozone differences in each grid cell of the 36 km CAMx modeling grid between the DEPMOD and BASE simulations at any time during June 2006. Note the different ozone scale in the two plots.

3.0 PERFORMANCE OF GLOBAL MODELS FOR THE GULF OF MEXICO

The TCEQ performs regional ozone modeling using the nested domains shown in Figure 3-1 (TCEQ, 2012). CAMx is run in 2-way nested mode for the 36, 12 and 4 km shown in red, blue and green. Boundary conditions for the red 36 km grid are extracted from a larger 36 km grid shown in grey called the RPO domain. Boundary conditions for the RPO domain are extracted from global model simulations. Both the GEOS-Chem (Bey et al., 2001) and MOZART4 (Emmons et al., 2010) global models have been used to provide boundary conditions for the RPO domain. TCEQ's "Rider 8" modeling for the month of June 2006 derives boundary conditions from GEOS-Chem.

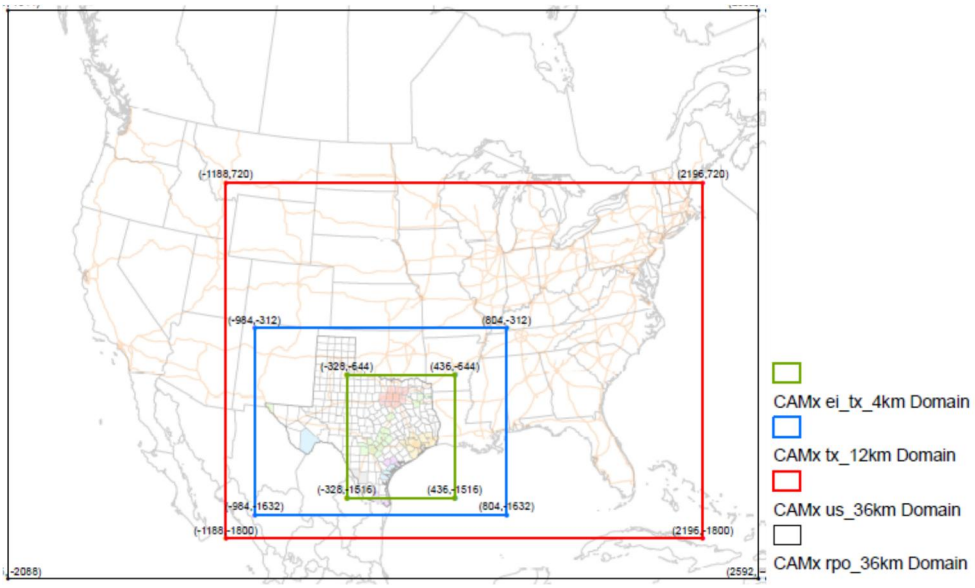

Figure 3-1. TCEQ's Rider 8 CAMx modeling domains.

Ozone over-prediction at Gulf Coast monitoring locations in TCEQ's Rider 8 modeling could result from GEOS-Chem over-predicting ozone at the boundaries of the CAMx RPO domain over the Gulf of Mexico and the tropical Atlantic Ocean. A previous evaluation of GEOS-Chem and MOZART4 found that both models tended to over-predict ozone by 10-15 ppb at Gulf Coast monitoring locations for the summers of 2005 and 2006 (Tai et al., 2009). A literature review was conducted to investigate GEOS-Chem, MOZART and other global models perform in simulating ozone in the Gulf Coast region.

3.1 Global Modeling for HTAP

At least 20 global models participated in modeling for the Task Force on Hemispheric Transport of Air Pollution (TF HTAP) interim assessment in 2007 (HTAP, 2007). HTAP operates under the United Nations Economic Commission for Europe (UNECE) Convention on Long-range Transboundary Air Pollution (LRTAP Convention) and is charged with assessing intercontinental transport of air pollutants such as ozone. The HTAP modeling results for ozone discussed by

Fiore et al. (2009) who evaluated source-receptor relationships between continents and by Reidmiller et al. (2009) for the influence of foreign vs. North American emissions on surface ozone in the U.S. Both Fiore et al. and Reidmiller et al. compared model predictions to observations at rural CASTNET ozone monitoring sites in the U.S. CASTNET sites used in model performance evaluation and located near the Gulf Coast are identified in Figure 3-2 from Reidmiller et al. The HTAP models and their main data sources are summarized in Table 3-1 from Fiore et al.

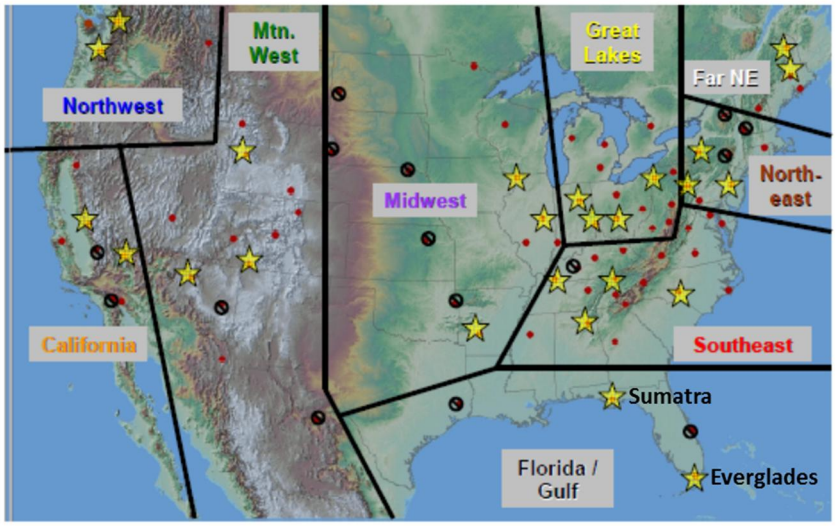

Figure 3-2. Map showing CASTNET monitoring sites used by Reidmiller et al. (2009) to evaluate global ozone model predictions. The Sumatra and Everglades sites are labeled and represented the Florida/Gulf region.

Table 3-1. Summary of the HTAP models and their main data sources (from Fiore et al. 2009).

Model	Grid Resolution (lon x lat x layers)	Institution	Anthropogenic emission inventory	Driving meteorology (year 2001)
CAMCHEM-3311m13	2.5ºx2ºx30	NCAR, USA	POET for 1997(a); CO fossil fuel and biofuel from a MOPITT inversion(b)	NCEP
ECHAM5-HAMMOZ-v21	2.81ºx2.81ºx21	EPFL, Switzerland	RETRO	ECMWF ERA-40
EMEP-rv26 (NH only)	1ºx1ºx20	EMEP, Norway	IER / Uni-Stuttgart, based on EDGAR2000; EMEP	ECMWF ERA-40
FRSGC/UCI v01	2.81ºx2.81ºx37	Lancaster University, UK	ACCENT/AR4(c)	ECMWF IFS(d)
GEMAQ-EC	2ºx2ºx20	Environment Canada	AURAMS (regional Canadian, US and Mexico); EDGAR	Canadian Meteorological Centre (CMC)

Model	Grid Resolution (lon x lat x layers)	Institution	Anthropogenic emission inventory	Driving meteorology (year 2001)
			elsewhere	
GEMAQ-v1p0	4ºx4ºx28	York University, Canada	EDGAR v2	CMC
GEOSChem-v07	2.5ºx2ºx30	Harvard University, USA	Bey et al., 2001(e)	NASA GEOS-4
GEOSChem-v07-res4x5	5ºx4ºx30	CIEMAT, Spain	EMEP emissions, EPA/NEI99 inventory	NASA GEOS-4
GISS-PUCCINI-modelA	5ºx4ºx23	NASA GISS, USA	As for modelE below	NCEP, via linear relaxation
GISS-PUCCINI-modelE	5ºx4ºx23	NASA GISS, USA	ACCENT/AR4, with EA emissions of CO and NOx times 1.66	NCEP, via linear relaxation
GMI-v02f	2.5ºx2ºx42	NASA GSFC, USA	Harvard's merged inventory (NEI99, BRAVO, Streets, EMEP)	NASA
LMDz3-INCA1	3.75ºx2.5ºx19	LSCE, France	RETRO	ECMWF ERA-40
LLNL-IMPACT-T5a	2.5ºx2ºx48	LLNL, USA	POET	NASA GEOS4-ceres
MOZARTGFDL-v2	1.88ºx1.88ºx28	GFDL, USA	EDGAR v2	NCEP
MOZECH-v16	2.81ºx2.81ºx31	FZ Julich, Germany	RETRO	ECMWF ERA-40
OsloCTM2	2.81ºx2.81ºx40	University of Oslo, Norway	EDGAR v3.2	ECMWF-IFS
STOC-HadAM3-v01	5ºx5ºx19	University of Edinburgh, UK	ACCENT/AR4	HadAM3GCM with observed 2001 SSTs and sea ice (PCMDI)
STOCHEM-HadGEM	3.75x2.5ºx20	Met Office, Hadley Centre, UK	ACCENT/AR4	HadGEM GCM with HadCM3 SSTs and sea ice
TM5-JRC-cy2-ipcc-v1	1ºx1ºx25	JRC, Italy	ACCENT/AR4	ECMWF
ULAQ-v02	5.625ºx5ºx26	Universita' degli Studi de L'Aquila, Italy	ACCENT/AR4	GCM with Hadley Centre SSTs
UM-CAM-v01	3.75ºx2.5ºx19	University of Cambridge, UK	ACCENT/AR4	GCM with Hadley Centre SST and sea ice (GISST 2.0)

The Sumatra and Everglades CASTNET monitoring sites were selected by Reidmiller et al. (2009) to represent the Florida/Gulf region. The left panel of Figure 3-3 shows observed daily maximum 8-hour average (MDA8) ozone at Sumatra (SUM) and Everglades (EVE) by month of 2001. Everglades has systematically lower MDA8 ozone than Sumatra because it is further removed than Sumatra from influence of continental ozone precursor emissions and closer to the equator where intense sunlight tends to cause ozone destruction in low-NOx environments. Both Sumatra and Everglades have springtime maximums and summer minimums in MDA8 ozone. The springtime ozone maximum is commonly seen at northern hemisphere background sites and results from long-lived ozone precursors (e.g., CO) accumulating over winter and then reacting in spring as solar radiation and temperatures increase. The right panel of Figure 3-3

compares model predicted MDA8 ozone to observations averaged over Sumatra and Everglades. The following points are noted:

- All models except for one (labeled INCA-vSSz) over-predict MDA8 ozone at Sumatra and Everglades from June to September.
- The multi-model mean over-predicts MDA8 ozone by 20 ppb or more at Sumatra and Everglades from June to September.
- The GEOS-Chem and MOZART model simulations for HTAP are close to the multi-model mean and therefore substantially over-predict MDA8 ozone at Sumatra and Everglades from June to September.

The INCA-vSSz model is of interest because it showed much better performance than all other HTAP models in simulating ozone for the Gulf Coast. The model labeled INCA-vSSz in Figure 3-3 is the LMDz-INCA model in Table 3-1 and is the general circulation model from the Laboratoire de Meteorologie Dynamique (LMD) coupled to the INteraction with Chemistry and Aerosols (INCA) chemistry scheme (Folberth et al., 2006) . vSSz appears to denote the lead researcher for LMDz-INCA in HTAP (Sophie Szopa; http://www.ipsl.jussieu.fr/~sszsce/).

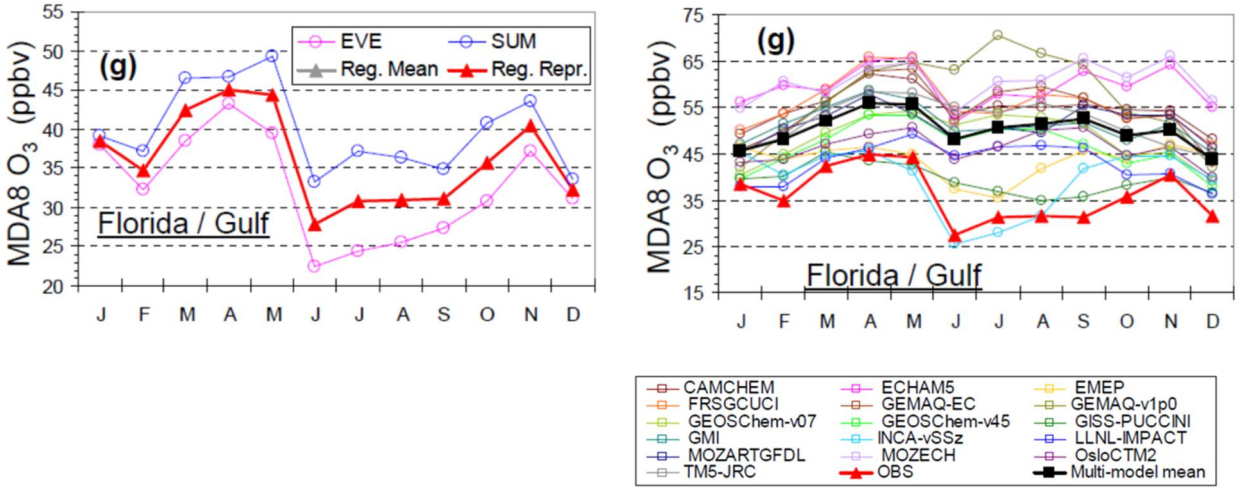

Figure 3-3. Daily maximum 8-hour average (MDA8) ozone at Sumatra (SUM), Everglades (EVE) and the mean of both sites by month of 2001 (left). Model predicted MDA8 ozone by month compared averaged over Sumatra and Everglades compared to the observed MDA8 (right) from Reidmiller et al. (2009).

3.2 LMDz-INCA, GEOS-Chem and MOZART

We reviewed documentation of LMDz-INCA (Folberth et al., 2006) seeking to identify model attributes that could explain how it out-performs GEOS-Chem and MOZART in simulating Gulf Coast ozone. As applied for HTAP (Table 3-1) had coarser horizontal resolution and fewer vertical layers (3.75ºx2.5ºx19) than either MOZART (1.88ºx1.88ºx28) or GEOS-Chem

(2.5ºx2ºx30). The INCA chemistry scheme for O_3 includes reactions of VOCs, NOx and CO with detail comparable to MOZART4 and GEOS-Chem. Reactions of halogens were not included in LMDz-INCA (or GEOS-Chem and MOZART) for HTAP simulations. LMDz-INCA used different anthropogenic emissions (RETRO; http://retro.enes.org/data_emissions.shtml) from GEOS-Chem and MOZART (EDGAR; http://edgar.jrc.ec.europa.eu/index.php). Both RETRO and EDGAR were developed at TNO in the Netherlands (http://www.tno.nl/) and are likely to contain similar emission estimates with the main difference being that RETRO provides historical emission estimates spanning 1960 to 2000. LMDz-INCA used different meteorology (ECMWF ERA-40; 40 year reanalysis project; http://www.ecmwf.int) from GEOS-Chem (NASA GEOS-4) and MOZART (NCEP). Several other HTAP models used ECMWF ERA-40 meteorology (ECHAM5, EMEP, MOZECH, TM5) and, although they are difficult to identify in Figure 3-3, appear to share with LMDz-INCA the prediction of a springtime ozone maximum followed by a summer minimum at Gulf Coast monitors (Figure 3-3). ECHAM5, EMEP, MOZECH, TM5 have a positive offset of ~20 ppb from LMDz-INCA in Figure 3-3 in disagreement with observations. This review suggests that the ECMWF ERA-40 meteorology may be one determining factor in the good performance of LMDz-INCA for ozone at Gulf Coast monitors.

Maps of global surface ozone predictions by LMDz-INCA from Folberth et al., (2006) are shown in Figure 3-4. In June-August (Figure 3-4) surface ozone shows sharp change between land and water along the coastline of the Gulf of Mexico. This feature is remarkable considering the coarse grid resolution (~300 km) of LMDz-INCA and it is difficult to understand how the model achieves this contrast. However, a good ability to distinguish between marine and continental air at the Gulf Coast (Figure 3-4) is consistent with the good performance of LMDz-INCA in simulating ozone at Sumatra and Everglades (Figure 3-3) and may be a second determining factor in the good performance of LMDz-INCA for ozone at Gulf Coast monitors.

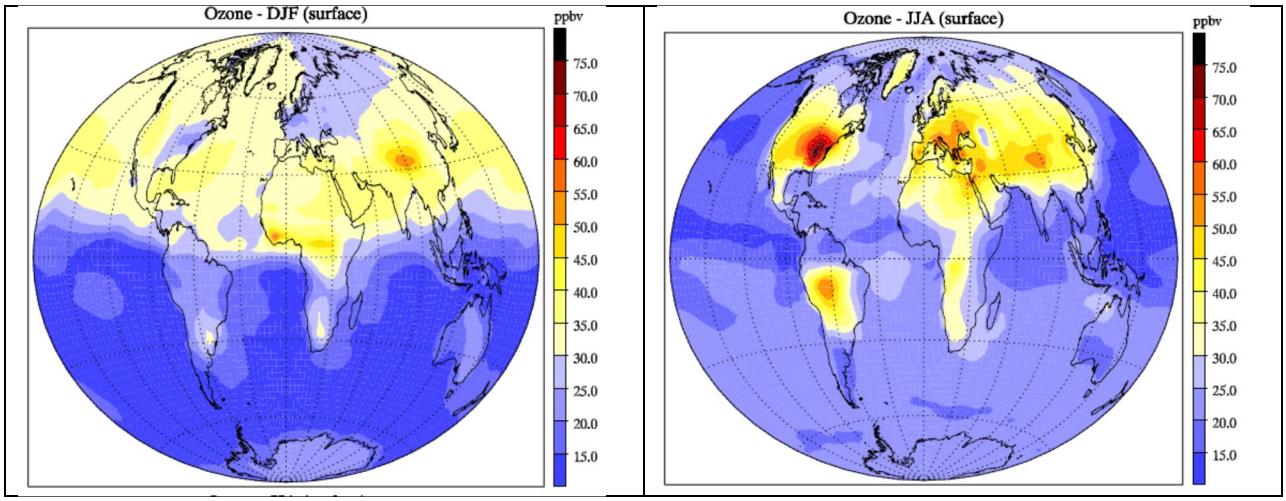

Figure 3-4. Surface ozone (ppb) for December-February (left) and June-August (right) in the LDMz-INCA global model (from Folberth et al. 2006).

Monthly time series of ozone from LMDz-INCA (Folberth et al. 2006), GEOS-Chem (Bey et al., 2001) and MOZART (Emmons et al., 2010) are compared in Figure 3-5 andFigure 3-6 using data published by model developers. Direct comparisons are not possible, but data were selected to investigate annual cycles of ozone at northern mid-latitude sites with continental and marine characteristics. For LMDz-INCA, Figure 3-5 shows surface ozone at two sites at latitude 34 N. LMDz-INCA is able to simulate the springtime maximum/summer minimum at the Azores in the mid-Atlantic and the summer maximum at Wallops Island which is dominated by outflow from North America. GEOS-Chem and MOZART were evaluated against ozone soundings rather than surface monitors, and so the highest pressure (lowest altitude) comparisons were selected. GEOS-Chem is able to simulate the springtime maximum/summer minimum at Kagoshima in southernmost Japan and (less well) the summer maximum at Boulder, CO. MOZART evaluation results are segregated by latitude band (equator to 30 N; 30 N to the North Pole) which combines influences of tropical vs. high-latitude photochemistry with increasing fraction of land area at northern high-latitudes. MOZART is fairly able to simulate the springtime maximum/summer minimum at equator to 30 N and the summer maximum at 30 N to the North Pole, although MOZART does not fully capture either the summer minimum or summer maximums. The comparisons in Figure 3-5 andFigure 3-6 suggest that all three models can represent different seasonal cycles in ozone that result either from proximity to the equator or continental vs. marine location.

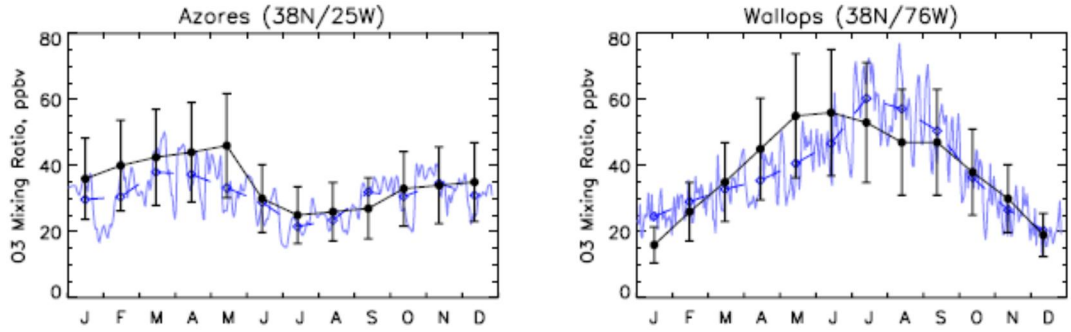

Figure 3-5. Monthly profiles of surface ozone (ppb) in the LDMz-INCA global model (black) and observed (blue) for two locations at 38 N: Wallops Island (in Virginia) and the Azores in the mid-Atlantic from Folberth et al. (2006).

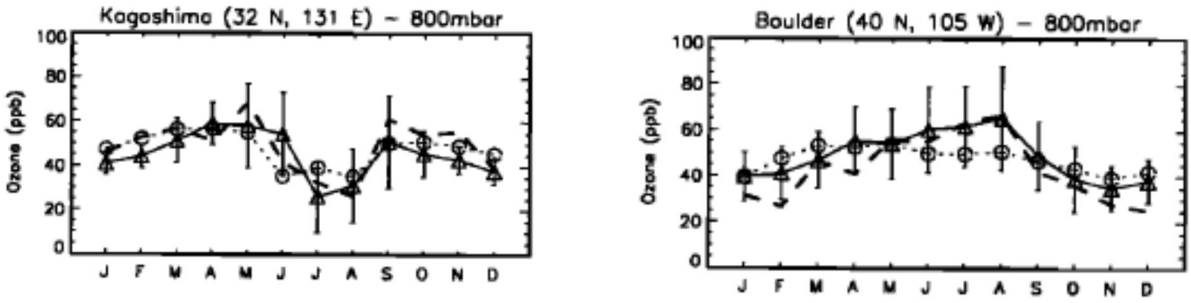

Figure 3-6. Monthly ozone (ppb) at 800 mb in the GEOS-Chem global model (open circles and dotted line) and observed (triangles with bars, solid line and dashed line) for Kagoshima (southernmost Japan) and Boulder (Colorado) from Bey et al. (2001).

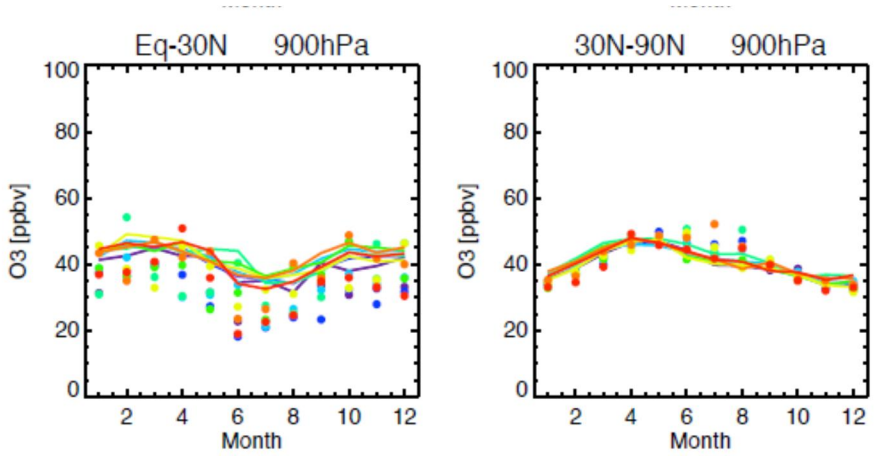

Figure 3-7. Monthly ozone (ppb) at 900 hPa in the MOZART4 global model (lines, 2000 to 2007 in different colors) and observed (dots, colors matching line years) for latitude bands equator to 30 N (average of 6 locations) and 30 N to 90 N (average of 21 locations) from Emmons et al. (2010).

The ability of GEOS-Chem and MOZART to distinguish marine air over the Gulf of Mexico from continental air was investigated by reviewing model output for June 2006. Ozone from the global models was reformatted to the TCEQ's Rider 8 CAMx 36 km grid using CAMx pre-processors. Surface ozone maps at noon CST on June 11-13, 2006, are shown in Figure 3-8. The GEOS-Chem to CAMx preprocessor assigns (rather than interpolates) concentrations and preserves the coarse grid resolution of GEOS-Chem in Figure 3-8. The MOZART to CAMx preprocessor interpolates concentrations and smoothes the coarse grid resolution of MOZART in Figure 8. Focusing on the Gulf Coast, both global models show a concentration gradient from higher ozone over land to lower over the Gulf, but the gradient is spread over several grid cells (500 km or greater). Keep in mind that the Gulf is ringed by land with several US states to the north, Florida to the east, Cuba and the Yucatan peninsula to the south and Mexico to the west. Consequently, only near the center of the Gulf can GEOS-Chem and MOZART represent air as being marine in character and not influenced by land-based emissions. Coarse model resolution

can explain why GEOS-Chem and MOZART over-predict summer ozone at Gulf Coast monitors. By extension, we expect that GEOS-Chem and MOZART over-predict ozone at the boundaries of the TCEQ's RPO CAMx 36 km grid (Figure 3-1) which could cause CAMx to over-predict ozone at Gulf Coast monitors.

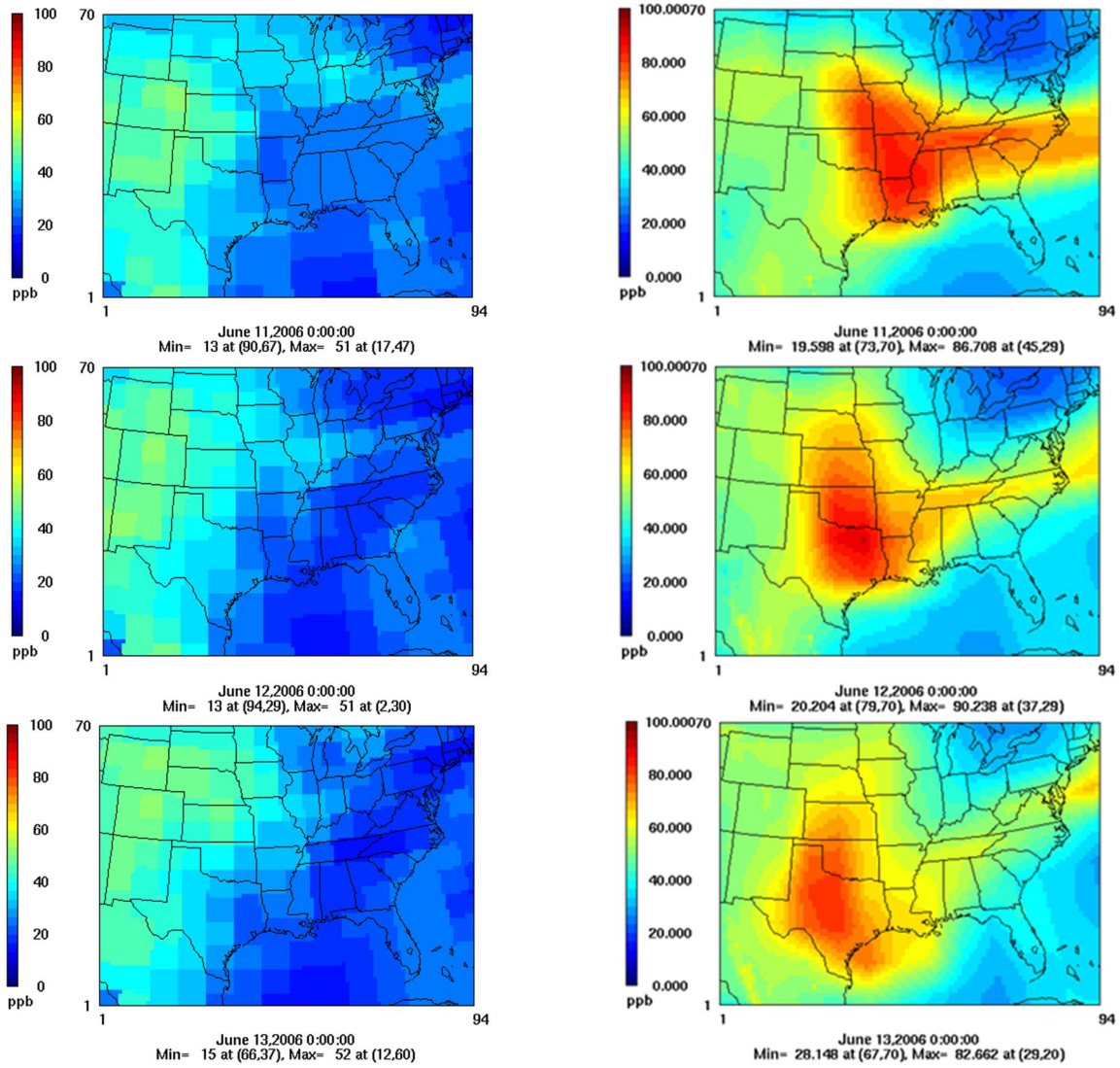

Figure 3-8. Ozone at noon CST on June 11-13, 2006, from GEOS-Chem (left) and MOZART4 (right) after being mapped to the TCEQ's Rider8 36 km grid by CAMx pre-processors.

3.3 CAMx Sensitivity Tests with Capped Boundary Conditions

We performed two CAMx sensitivity tests using the June 2006 Rider 8 model with lowered boundary conditions (BCs) over the Gulf of Mexico and Atlantic Ocean. The BCs were revised by placing upper limits (caps) on concentrations in each layer. The caps were applied by species (O_3, NO_2, etc.) to the June 2006 average GEOS-Chem concentrations at the southeast corner of the RPO domain (Figure 3-1). The first test (BC Scen) capped only ozone and the second test (BC

Scen2) capped both ozone and precursor concentrations. The O_3 cap was 22 ppb in the CAMx surface layer and rose with altitude.

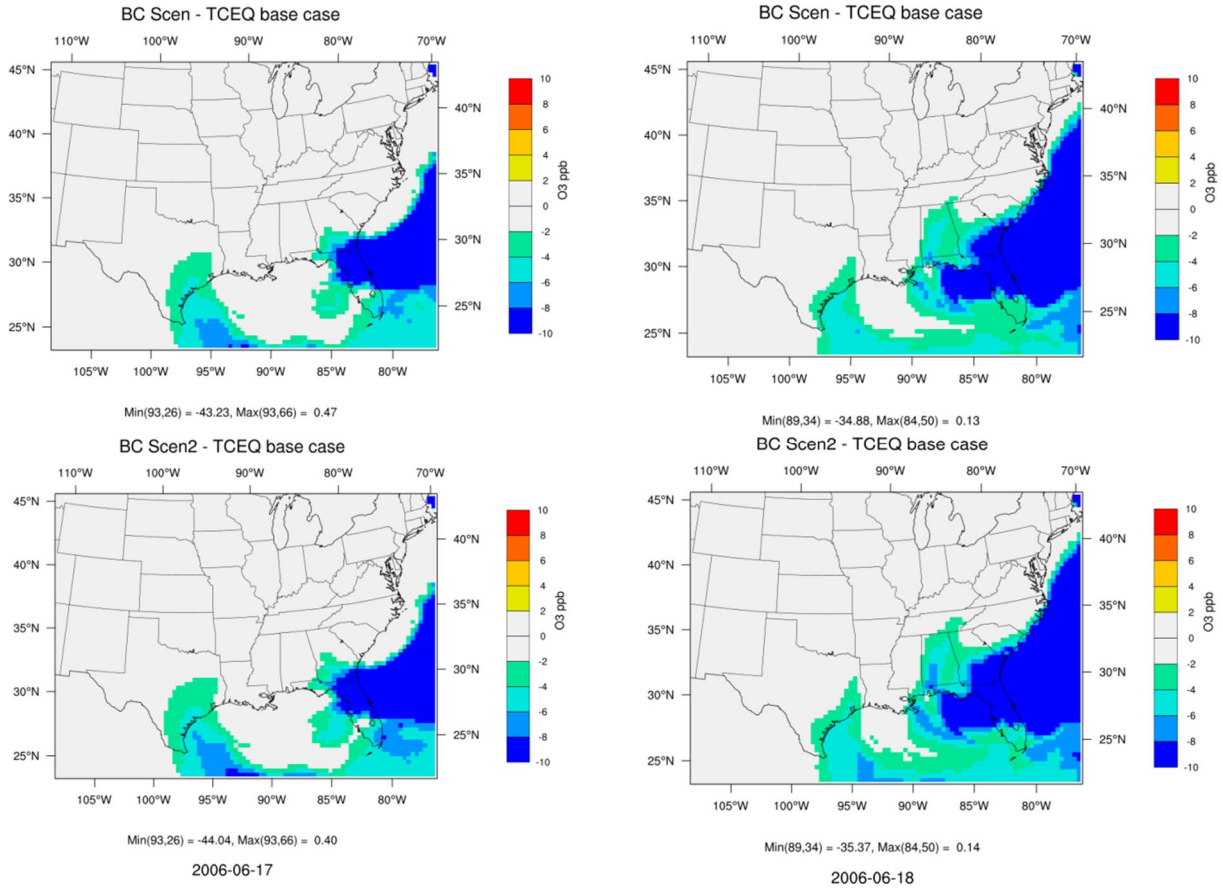

Figure 3-9. Difference in MDA8 ozone on June 17 and 18, 2006 (left and right) due to capping the BCs over the Gulf of Mexico and Atlantic Ocean. Test BC Scen (upper) capped only ozone and test BC Scen2 (lower) capped both ozone and precursor concentrations.

Results of the BC sensitivity tests are shown in Figure 3-9 for two days with persistent on-shore flow (June 17 and 18, 2006). Ozone differences are shown as changes (reductions) in the daily maximum 8-hour average (MDA8). Capping the BCs reduced ozone over large areas of the Atlantic Ocean and Gulf of Mexico with reductions transported on-shore in some places. Comparing the two scenarios shows that capping BC ozone produced the majority of reductions.

In test BC Scen (ozone BCs capped), large reductions in DMA8 ozone (up to 43 ppb) occur near the eastern domain boundary over the Atlantic Ocean and are associated with reductions over land exceeding 10 ppb in Florida, southern Georgia and in the Gulf of Mexico near Florida's panhandle where the Sumatra monitor is located (Figure 3-2). Near the southern boundary over the Gulf of Mexico reductions in MDA8 ozone are in the range 5 – 10 ppb and are associated with reductions over land exceeding 4 ppb along the Texas Gulf Coast including Galveston.

3.4 Conclusion

Ozone concentrations at the boundaries of TCEQ's CAMx domain are extracted from global simulations performed using the GEOS-Chem (Bey et al., 2001) or MOZART4 (Emmons et al., 2010) models. A previous evaluation of GEOS-Chem and MOZART4 found that both models tended to over-predict ozone by 10-15 ppb at Gulf Coast monitoring locations for the summers of 2005 and 2006 (Tai et al., 2009). Over 20 global models, including GEOS-Chem and MOZART4, were evaluated for their performance in simulating Gulf Coast ozone in studies for the Task Force on Hemispheric Transport of Air Pollution (HTAP) 2007 interim assessment (Fiore et al., 2009; Reidmiller et al., 2009). All models but one (the LMDZ-INCA model from France) over-predicted Gulf Coast ozone from June to September by ~20 ppb on average. The formulation of the LMDZ-INCA model (Folberth et al., 2006) is not substantially different from other models although the driving meteorology (ECMWF ERA-40 data) may partly explain why LMDz-INCA performed well.

Most global models, including GEOS-Chem and MOZART4, employ horizontal grid resolutions of several hundred km. The ability of GEOS-Chem and MOZART to distinguish marine air over the Gulf of Mexico from continental air was investigated by reviewing model output for June 2006. Both models show a concentration gradient from higher ozone over land to lower over the Gulf, but the gradient is spread over several grid cells (500 km or greater). Keep in mind that the Gulf is ringed by land with several US states to the north, Florida to the east, Cuba and the Yucatan peninsula to the south and Mexico to the west. Consequently, only near the center of the Gulf can GEOS-Chem and MOZART represent air as being marine in character and not influenced by land-based emissions. Coarse model resolution can explain why GEOS-Chem and MOZART over-predict summer ozone at Gulf Coast monitors. By extension, we expect that GEOS-Chem and MOZART over-predict ozone at the boundaries of the TCEQ's CAMx grid. A sensitivity test with reduced ozone at the CAMx boundaries over the Gulf and the Atlantic showed that ozone high bias in GEOS-Chem can influence CAMx ozone at Gulf Coast monitors by 5 – 10 ppb.

4.0 OZONE DEPLETION BY IODINE

Atmospheric reactions of iodine atoms (I-atoms) can destroy tropospheric ozone through series of chemical reactions such as the IO + HO2 cycle (Chameides and Davis, 1980) shown below.

IO + HO_2 cycle		*IO + IO cycle*		*IO + NO_2 cycle*	
$I + O_3 \rightarrow IO + O_2$		$(I + O_3 \rightarrow IO + O_2) \times 2$		$I + O_3 \rightarrow IO + O_2$	
$IO + HO_2 \rightarrow HOI + O_2$		$IO + IO \rightarrow I + OIO$		$IO + NO_2 \rightarrow IONO_2$	
$HOI + h\nu \rightarrow I + OH$		$OIO + h\nu \rightarrow I + O_2$		$IONO_2 + h\nu \rightarrow I + NO_3$	
Net: $O_3 + HO_2 \rightarrow OH + 2\ O_2$	Net:	$2\ O_3 \rightarrow 3\ O_2$		$NO_3 + h\nu \rightarrow NO + O_2$	
				$NO + O_3 \rightarrow NO_2 + O_2$	
			Net:	$2\ O_3 \rightarrow 3\ O_2$	

These reactions are referred to as catalytic cycles because the I-atom is regenerated in the reactions and therefore one I-atom can potentially destroy many O_3 molecules. I-atoms and iodine monoxide (IO) are rapidly interconverted by these reactions such that is useful to consider them collectively (I + IO) as reactive iodine. The IO + IO and IO + NO_2 cycles differ in the reactions that convert IO back to I-atom (Mahajan et al., 2009).

The efficiency of tropospheric O_3 destruction by reactive iodine (i.e., the number of O_3 molecules destroyed per I-atom) depends upon how effectively reactive iodine species are eliminated by other reactions. For example, the self-reaction of IO produces a larger iodine oxide (I_2O_2) that may become a sink for reactive iodine (Saunders and Plane, 2005; Sommariva et al., 2012).

$$IO + IO \rightarrow 0.4\ I + 0.4\ OIO + 0.6\ I_2O_2$$

I_2O_2 formation in the IO self-reaction of competes against conversion of IO back to I-atom in the catalytic cycles that destroy O_3.

Larger iodine oxides (I_2O_3, I_2O_4, I_2O_5 etc.; collectively, IxOy) can form aerosols and thus remove iodine from the gas-phase. Details of I-containing aerosol formation remain uncertain (Sommariva et al., 2012; but reactions of IO and iodine dioxide (OIO) are believed to be involved. Iodic acid (HIO_3) also is believed to be involved in the formation of I-containing aerosols. Iodine aerosols have been studied extensively because they are an important source of new particles in marine environments.

Catalytic destruction of O_3 by reactive iodine may be interrupted by formation of reservoir species, for example when an I-atom is added to a nitrogen oxide NO, NO_2 or NO_3:

$$I + NO \rightarrow INO$$
$$I + NO_2 \rightarrow INO_2$$
$$I + NO_3 \rightarrow INO_3$$

The resulting compounds (collectively, INOy) are temporary iodine reservoirs because they are destroyed by photolysis and/or chemical reactions that return the iodine to an active form. Other potential reservoir species for reactive iodine include HI and HOI.

Emissions from oceans are the major source of atmospheric iodine (Carpenter, 2003) with emitted compounds including methyl iodide (CH_3I), other iodo-methanes (CH_2I_2, CH_2ICl, CH_2IBr), larger alky iodides and molecular iodine (I_2; Saiz-Lopez and Plane, 2004). Iodine emissions result both from biological (Moore and Tokarczyk, 1993) and photochemical (Moore and Zafirou, 1996) processes in ocean water. Photochemical processes that cause iodine emissions are linked to reactions of dissolved O_3 and thereby to enhanced O_3 deposition to oceanic waters (Ganzeveld et al., 2009; Helmig et al., 2012).

CH_3I is destroyed mainly by photolysis, liberating an I-atom, with an atmospheric lifetime of several days (Atkinson et al., 2010). Photolysis of larger alkyl iodides is faster than CH_3I by a about a factor of 2 (Cotter et al., 2001). Photolysis the other iodo-methanes and I_2 occurs in minutes (Atkinson et al., 2010).

4.1 Iodine Mechanism

ENVIRON developed a chemical mechanism for iodine and ozone that is suitable for use in regional photochemical modeling of ozone in Texas as shown in Tables A-D. The chemical reactions included in the mechanism (Table 4-1) are based primarily on the recent review by Sommariva et al. (2012) and making reference to other recent studies by Ordonez et al. (2012) and Mahajan et al. (2010). The citations given for each reaction in Table 4-1 indicate the data source. The model species names used in Table 4-1 are defined in Table 4-2.

Table 4-1. Listing of the chemical mechanism for iodine and ozone.

Number	Reactants and Products	k_{298}	Rate Parameters			Notes
			A	E_a	B	
I1	I + O3 = IO	1.30E-12	2.10E-11	830.0	0.00	a
I2	I + HO2 = HI	3.87E-13	1.50E-11	1090.0	0.00	a
I3	I + NO = INO	3.76E-13	Falloff, F=0.60 ,N=1.00			a
		k_0	1.80E-32	0.0	-1.00	
		k_∞	1.70E-11	0.0	0.00	
I4	I + NO2 = INO2	5.24E-12	Falloff, F=0.63 ,N=1.00			a
		k_0	3.00E-31	0.0	-1.00	
		k_∞	6.60E-11	0.0	0.00	
I5	I2 = 2 I	Photolysis				a
I6	I2 + OH = HOI + I	2.10E-10	2.10E-10			a
I7	I2 + NO3 = I + INO3	1.50E-12	1.50E-12			a
I8	HI + OH = I	7.00E-11	1.60E-11	-440.0	0.00	
I9	IO = I + O	Photolysis				a
I10	IO + NO = I + NO2	1.96E-11	7.15E-12	-300.0	0.00	a
I11	IO + NO2 = INO3	3.55E-12	Falloff, F=0.40 ,N=1.00			a
		k_0	7.70E-31	0.0	-5.00	
		k_∞	1.60E-11	0.0	0.00	
I12	IO + HO2 = HOI	8.57E-11	1.40E-11	-540.0	0.00	a

Number	Reactants and Products	k_{298}	Rate Parameters			Notes
			A	E_a	B	
I13	IO + IO = 0.4 I + 0.4 OIO + 0.6 I2O2	9.88E-11	5.40E-11	-180.0	0.00	a,b
I14	HOI = I + OH	Photolysis				a
I15	HOI + OH = IO	5.00E-12	5.00E-12			c
I16	OIO = I	Photolysis				d
I17	OIO + NO = IO + NO2	6.78E-12	1.10E-12	-542.0	0.00	a
I18	OIO + OH = HIO3	4.72E-10	Falloff, F=0.30 ,N=1.00			e
		k_0	1.50E-27	0.0	-3.93	
		k_∞	5.50E-10	-46.0	0.00	
I19	OIO + IO = IXOY	1.00E-10	1.00E-10			f
I20	OIO + OIO = IXOY	1.50E-10	1.50E-10			f
I21	I2O2 = I + OIO	1.00E+01	1.00E+01			g
I22	I2O2 + O3 = IXOY	1.00E-12	1.00E-12			h
I23	INO + I = I2 + NO	1.66E-10	1.66E-10			i
I24	INO + INO = I2 + 2 NO	1.28E-14	8.40E-11	2620.0	0.00	a
I25	INO2 = I + NO2	Photolysis				a
I26	INO2 + INO2 = I2 + 2 NO2	1.73E-15	4.70E-13	1670.0	0.00	a
I27	INO3 = I + NO3	Photolysis				j
I28	INO3 + I = I2 + NO3	5.58E-11	9.10E-11	146.0	0.00	g
I29	CH3I = I + MEO2	Photolysis				a
I30	MI2 = 2.000 I + FORM	Photolysis				a
I31	MIB = I + XO2 + FORM	Photolysis				a
I32	MIC = I + XO2 + FORM	Photolysis				a
I33	IALK = I + XO2H + ALDX	Photolysis				a,k

Table notes:

k_{298} is the rate constant at 298 K and 1 atmosphere using units of molecules cm^{-3} and s^{-1}

See Table 4-2 for species names

See Table 4-3 for information on photolysis reactions

MEO2, FORM and ALDX in reactions I29 – I33 are Carbon Bond species names and should be changed for use with a different base mechanism

References are indicated in the notes column as follows:

a	Atkinson et al. (2010) – IUPAC	e	Plane et al. (2006)	i	van den Bergh et al. (1976)
b	Sommariva et al. (2012)	f	Gomez-Martin et al. (2007)	j	Joseph et al. (2007)
c	Riffault et al. (2005)	g	Kaltsoyannis et al. (2008)	k	Taatjes et al. (2012)
d	Sander et al. (2011) – JPL	h	Saunders et al. (2005)	l	Cotter et al. (2001)

Notable differences between the mechanisms in Table 4-1 and Sommariva et al. (2012) are:

- Inclusion of reaction I23 (INO + I) which strongly limits daytime accumulation of INO.
- Inclusion of photolysis reactions I30 to I33 for iodocarbons in addition to CH_3I (reaction I30).
- Condensation of the reactions forming iodine oxides larger than I_2O_2 to a single species IXOY which is defined as containing two I-atoms.
- Exclusion of a reaction between IO and CH_3O_2 which is uncertain (Sommariva et al., 2012) and did not have a large impact on model results (discussed below).

Table 4-2. Model species names and properties in the chemical mechanism for iodine and ozone.

Model Species Name	Description	Chemical Formula							M. Wt. (g)	Henry Constant		
		C	H	O	N	Cl	Br	I		H_{298} ($M\ atm^{-1}$)	A (K)	Notes
I2	molecular iodine							2	253.8	3.10E+00	-4600	
I	iodine atom							1	126.9	8.00E-02	-2300	
IO	iodine monoxide			1				1	142.9	8.00E-02	-2300	Same as I
OIO	iodine dioxide			2				1	158.9	1.00E+00	-3300	Same as OClO
I2O2	diiodine dioxide			2				2	285.8	1.00E+06	-4000	Large value
IXOY	condensable iodine oxides			3				2	301.8	1.00E+06	-4000	Large value
HI	hydrogen iodide		1					1	127.9	1.00E+06	-9800	Accounting for dissociation
HOI	hypoiodous acid		1	1				1	143.9	4.10E+02	-4000	
HIO3	iodic acid		1	3				1	175.9	1.00E+06	-4000	
INO	nitrosyl iodide			1	1			1	156.9	5.00E-02	-4000	Same as ClNO
INO2	nitryl iodide			2	1			1	172.9	3.00E-01	-4000	Same as $BrNO_2$
INO3	iodine nitrate			3	1			1	188.9	1.00E+06	-4000	Same as $BrNO_3$ (large)
CH3I	iodomethane	1	3					1	141.9	1.40E-01	-4300	
MIC	chloroiodomethane	1	2			1		1	176.4	8.90E-01	-4300	
MIB	bromoiodomethane	1	2				1	1	219.9	8.90E-01	-4300	Same as CH_2ICl
MI2	diiodomethane	1	2					2	267.8	2.30E+00	-5000	
IALK	alkyl iodides	3	7					1	170.0	6.30E-02	-4000	

Table notes:
H_{298} is the Henry Constant at 298 K and T factor is the temperature dependence (K)
Henry constant data from http://www.mpch-mainz.mpg.de/~sander/res/henry.html
Henry constants are for the exact compound unless noted otherwise under comments
Default value for temperature dependence (A) is 4000 K

4.2 Photolysis Rates

Photolysis rates for species included in the iodine mechanism (Table 4-1) were calculated using the TUV radiative transfer model for representative atmospheric conditions as shown in Table 4-3. Frequently it is useful to characterize the photolysis rate for one reaction as a ratio to another reaction, although the reference reaction should be selected so that the ratio has little dependence upon zenith angle. Photolysis rate ratios for iodine compounds are listed below with the reference reactions defined in the footnote to Table 4-3.

j(I2)	=	0.922	x	j(NO3_NO2)
j(IO)	=	18.5	x	j(NO2)
j(OIO)	=	0.907	x	j(NO3_NO2)
j(HOI)	=	10.1	x	j(NO2)
j(INO2)	=	0.509	x	j(NO2)

i(INO3)	=	522.2	x	j(FORM_M)
j(CH3I)	=	1.15	x	j(HNO3)
j(MI2)	=	198.2	x	j(FORM_M)
j(MIB)	=	14.2	x	j(FORM_R)
j(MIC)	=	4.21	x	j(FORM_R)
j(IALK)	=	2.31	x	j(HNO3)

Table 4-3. Photolysis rates (s^{-1}) for iodine-containing species and reference reactions.

Species Name	Solar Zenith Angle (degrees)									
	0	10	20	30	40	50	60	70	78	86
I2	1.51E-01	1.50E-01	1.47E-01	1.43E-01	1.36E-01	1.27E-01	1.12E-01	8.88E-02	5.80E-02	1.35E-02
IO	1.72E-01	1.72E-01	1.67E-01	1.60E-01	1.50E-01	1.34E-01	1.12E-01	8.00E-02	4.48E-02	1.10E-02
OIO	1.48E-01	1.47E-01	1.45E-01	1.41E-01	1.34E-01	1.25E-01	1.11E-01	8.78E-02	5.75E-02	1.30E-02
HOI	9.55E-02	9.47E-02	9.22E-02	8.78E-02	8.12E-02	7.17E-02	5.87E-02	4.05E-02	2.20E-02	5.60E-03
INO2	4.83E-03	4.78E-03	4.65E-03	4.43E-03	4.08E-03	3.60E-03	2.93E-03	2.02E-03	1.09E-03	2.80E-04
INO3	2.40E-02	2.38E-02	2.28E-02	2.12E-02	1.88E-02	1.58E-02	1.18E-02	7.18E-03	3.50E-03	9.60E-04
CH3I	7.82E-06	7.65E-06	7.15E-06	6.33E-06	5.25E-06	3.98E-06	2.62E-06	1.33E-06	5.50E-07	1.26E-07
IALK	1.56E-05	1.53E-05	1.43E-05	1.27E-05	1.05E-05	7.97E-06	5.22E-06	2.65E-06	1.10E-06	2.52E-07
MI2	9.33E-03	9.20E-03	8.78E-03	8.07E-03	7.07E-03	5.75E-03	4.15E-03	2.40E-03	1.11E-03	2.87E-04
MIB	5.93E-04	5.83E-04	5.52E-04	5.02E-04	4.30E-04	3.42E-04	2.38E-04	1.32E-04	5.92E-05	1.47E-05
MIC	1.78E-04	1.75E-04	1.65E-04	1.48E-04	1.26E-04	9.90E-05	6.82E-05	3.70E-05	1.63E-05	3.98E-06
NO2	9.58E-03	9.50E-03	9.22E-03	8.73E-03	8.02E-03	7.00E-03	5.60E-03	3.73E-03	1.95E-03	5.27E-04
NO3_NO2	1.63E-01	1.62E-01	1.60E-01	1.55E-01	1.48E-01	1.38E-01	1.22E-01	9.70E-02	6.37E-02	1.46E-02
FORM_R	4.17E-05	4.10E-05	3.88E-05	3.53E-05	3.05E-05	2.42E-05	1.68E-05	9.08E-06	3.95E-06	9.20E-07
FORM_M	4.63E-05	4.58E-05	4.38E-05	4.07E-05	3.60E-05	2.98E-05	2.20E-05	1.31E-05	6.27E-06	1.68E-06
HNO3	6.77E-06	6.62E-06	6.20E-06	5.50E-06	4.57E-06	3.45E-06	2.25E-06	1.12E-06	4.43E-07	9.28E-08

Table notes:

Rates calculated for an ozone column of 300 Dobson units, surface albedo of 0.04, and height above ground of 640 m

NO3_NO2 means NO_3 photolysis producing NO_2

FORM_R means formaldehyde photolysis producing radical products (HCO + H)

FORM_M means formaldehyde photolysis producing molecular products (CO + H_2)

4.3 Deposition Velocities

Data required to implement chemical species in the CAMx algorithms for dry and wet deposition (ENVIRON, 2012) include the Henry Constant (for gas-aqueous partitioning) and molecular weight (for molecular diffusivity) as listed in Table 4-2. Molecular weights were calculated from the molecular formulas. Henry Constants were selected from the data compilation by Sander (http://www.mpch-mainz.mpg.de/~sander/res/henry.html) and where the compilation reported several values we favored recent data and experiments over computations. In some instances Henry Constants were set to values reported for similar molecules. The temperature dependence of the Henry Constant (H_T) is defined by the expression:

$$H_T = H_{298} \exp\left[A\left(\frac{1}{298} - \frac{1}{T}\right)\right]$$

where A is the temperature dependence in units of K. Where no temperature dependence was available for the Henry Constant we assumed a default value of -4000 K.

4.4 Emissions of Iodine Compounds

ENVIRON developed a CAMx pre-processor to estimate oceanic emissions of iodine compounds. Emissions from seawater of volatile organo-iodine (VOI) compounds including CH_3I, CH_2I_2 (MI2), CH_2ICl (MIC), CH_2IBr (MIB) were estimated using the method proposed by Ordonez et al. (2012) whereby emission rates are proportional to the water content of chlorophyll-a (units of mg/m^3). The SeaWiFS satellite provides chlorophyll-a data with global coverage as monthly averages, as illustrated in Figure 4-1. The CAMx pre-processor projects the satellite data to a CAMx grid and excludes chlorophyll-a detected in freshwater lakes, as illustrated in Figure 4-2. The VOI compound emission factors were set to reproduce global emission budgets reported for CH_3I (213 Gg/yr; Bell et al., 2002), CH_2I_2 (116 Gg/yr; Ordonez et al. 2012), CH_2ICl (234 Gg/yr; Ordonez et al. 2012) and CH_2IBr (87,3 Gg/yr; Ordonez et al. 2012). Emissions of I_2 from seawater were set to a constant emission flux of 4×10^8 molecule cm^{-2} s^{-1} which is between the estimates of Sommariva et al. 2009 (1.2×10^9 molecule cm^{-2} s^{-1} for the remote marine boundary layer) and Mahajan et al. 2010 (5×10^7 molecule cm^{-2} s^{-1}).

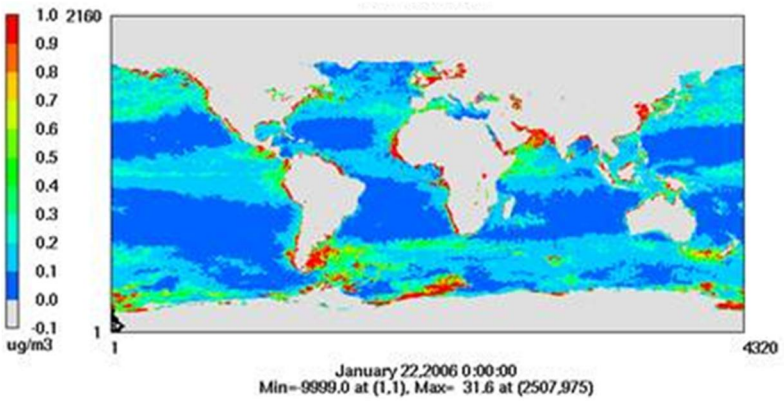

Figure 4-1. Example global coverage of chlorophyll-a (units of mg/m^3) from SeaWiFS satellite data. Note that chlorophyll-a is detected in freshwater lakes.

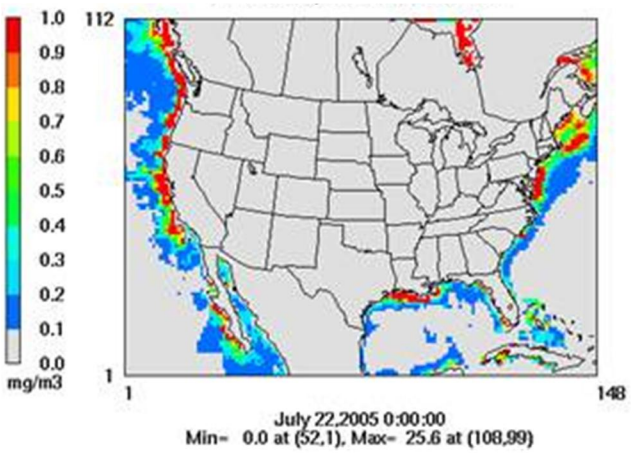

Figure 4-2. Example coverage of chlorophyll-a (units of mg/m^3) projected to a CAMx grid. Note that chlorophyll-a in freshwater lakes has been excluded.

4.5 CAMx Simulation Results

The iodine-ozone mechanism was integrated with CB6 in CAMx and tested using the Rider 8 modeling database developed by TCEQ for June 2006. Oceanic emissions of iodine compounds (I_2 and VOIs) were estimated using the CAMx emissions pre-processor described above. The resulting ozone differences are shown in Figure 4-3 for two days with persistent on-shore flow in Texas (June 17 and 18, 2006). Ozone differences are shown as changes (reductions) in the daily maximum 8-hour average (MDA8). Reductions in MDA8 ozone of about 5 ppb occur over large areas of the Gulf of Mexico and in the Atlantic Ocean offshore of Virginia to Massachusetts. Ozone reductions can be transported onshore, especially in Florida and the Gulf Coast States including Texas. Ozone reductions are smaller onshore than offshore because the boundary layer deepens and is diluted as air moves onshore and because iodine emissions were from ocean waters.

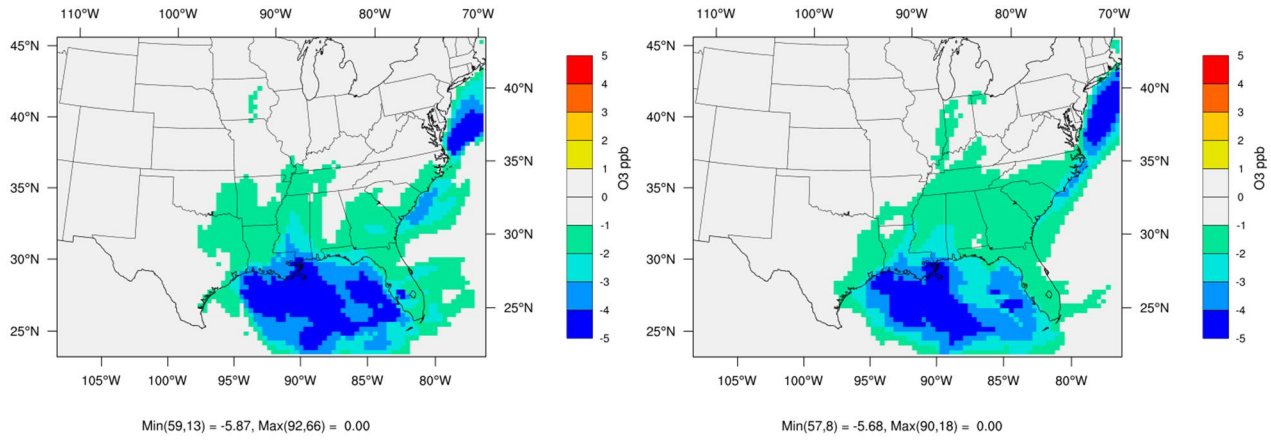

Figure 4-3. Difference in MDA8 ozone on June 17 and 18, 2006 (left and right) due to oceanic emissions and reactions of iodine compounds (with iodine – without iodine).

The distribution of iodine among iodine-containing species is shown for Galveston in Figure 4-4 and Table 4-2. The average diurnal profiles of iodine-containing species for June 2006 were computed from the CAMx predictions at Galveston. The most abundant iodine precursor is CH_3I (monthly average concentration of 1.65 ppt) because it's chemical lifetime is longer than other iodine precursors. Iodine accumulates in the aerosol phase mainly as higher iodine oxides (IxOy; 10.2 ppt) rather than iodic acid (HIO_3; 3.2 ppt). The reservoir species INO_3 (11.5 ppt) and INO_2 (6.2 ppt) carry significant iodine concentrations at Galveston with INO_3 being depleted by photolysis during daylight whereas INO_2 peaks during daylight. The main reactive iodine species is IO with the average diurnal profile having a maximum concentration of 1.7 ppt for IO, which is comparable to measurements at the Cape Verde Islands in the tropical Atlantic Ocean (Mahajan et al., 2010).

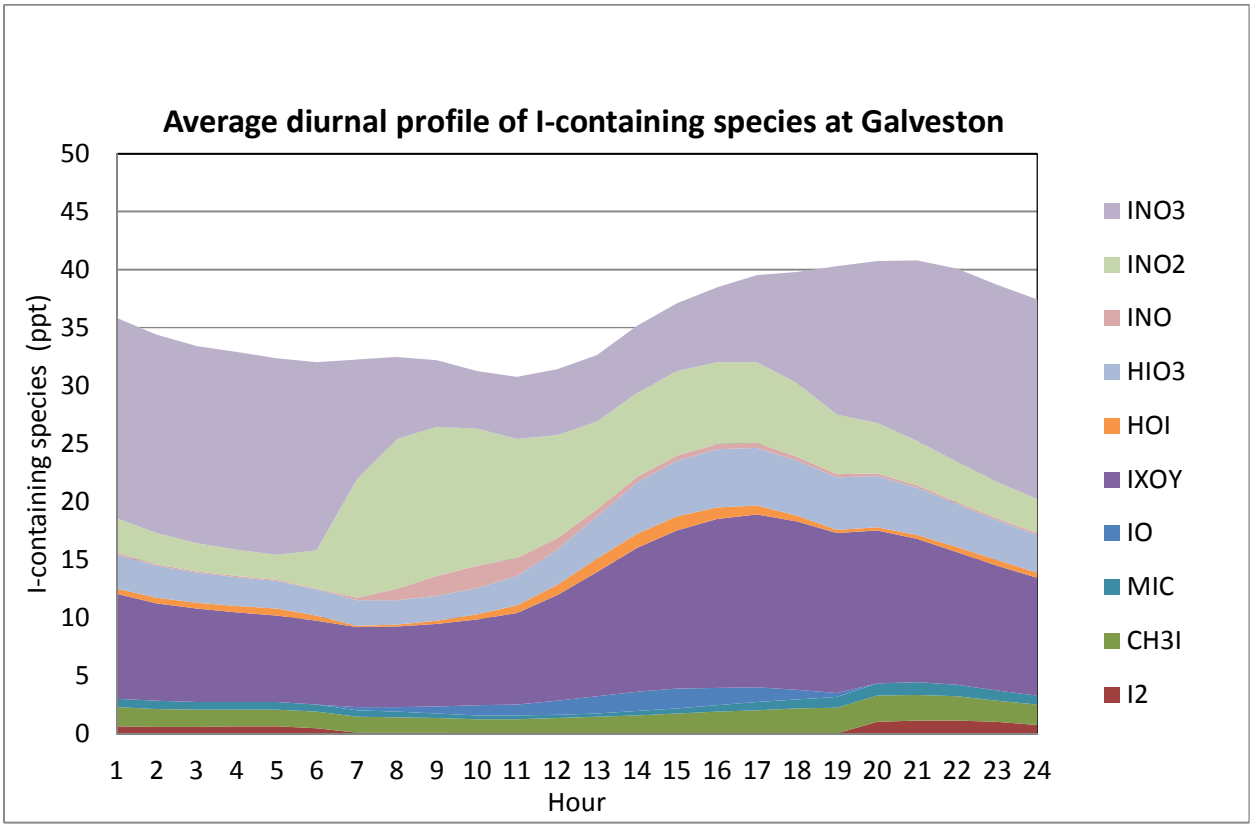

Figure 4-4. The average diurnal concentration profile (ppt) of iodine-containing species predicted by CAMx at Galveston for June 2006. Species containing less than 1% of total iodine are omitted.

Table 4-4. The average concentration of iodine-containing species and the maximum of the average diurnal concentration profile predicted by CAMx at Galveston for June 2006.

Species	Average concentration (ppt)	Maximum of average diurnal concentration profile (ppt)
Precursors		
I2	0.38	1.16
CH3I	1.65	2.24
MI2	0.099	0.240
MIC	0.64	1.07
MIB	0.150	0.282
Reactive Iodine		
I	0.109	0.319
IO	0.547	1.70
OIO	0.010	0.032
I2O2	0.00009	0.00032
Particulate Iodine		
IXOY	10.2	14.9
HIO3	3.36	4.99
Reservoir Species		
INO	0.50	1.91
INO2	6.2	12.9
INO3	11.5	17.3
HI	0.044	0.094
HOI	0.57	1.25

4.5.1 Iodine Mechanism Sensitivity Test

Dillon et al. (2006, 2010) report that IO reacts with methyl peroxy radical (CH_3O_2) but Sommariva et al. (2012) comment that both the rate constant and products are uncertain for this reaction. A sensitivity test was conducted including this reaction with a rate constant of 2 x 10^{-12} cm^3 $molecule^{-1}$ $s^{-1}$and products I + CH_3O (IO + MEO2 → I + HO2 + FORM in CB6). The resulting changes in MDA8 O_3 shown in Figure 4-5 are less than 0.1 ppb which compares with changes in MDA8 O_3 due to the iodine-ozone mechanism of 5 ppb shown in Figure 4-3. Therefore, reaction of IO with CH_3O_2 was omitted from the final iodine-ozone mechanism. By extrapolation from this result, reactions of IO with other RO_2 radicals were omitted.

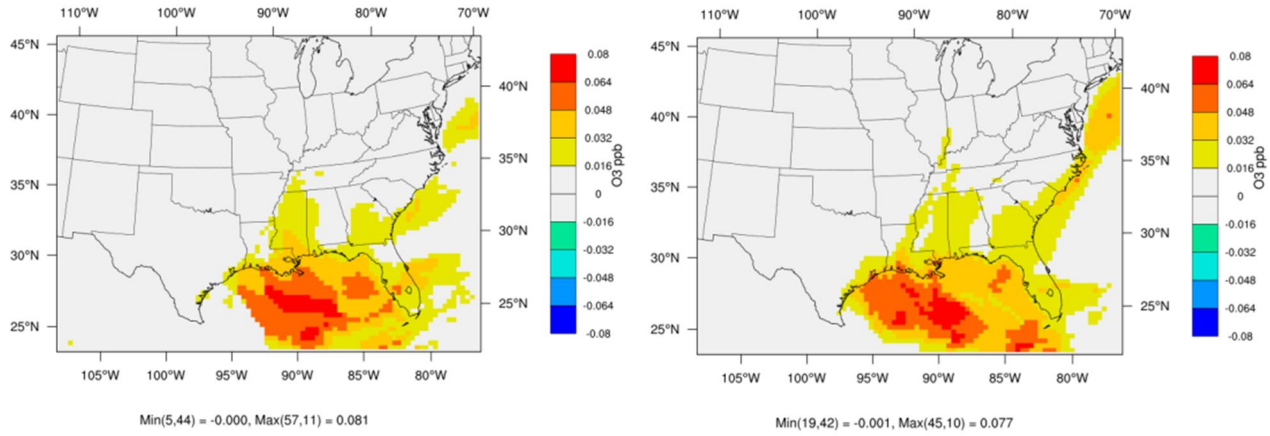

Figure 4-5. Sensitivity of MDA8 ozone on June 17 and 18, 2006 (left and right) to the reaction IO + MEO2 → I + HO2 + FORM (with reaction – without reaction). The reaction is omitted from the final mechanism.

4.6 Conclusion

Atmospheric reactions of iodine atoms deplete ozone catalytically, meaning that a single iodine atom can destroy many ozone molecules (Chameides and Davis, 1980; Mahajan et al., 2009). Iodine compounds are emitted from ocean waters through biological and photochemical mechanisms and the oceans are the largest source of atmospheric iodine (Carpenter, 2003). Several field studies and numerous laboratory experiments have investigated how iodine depletes ozone and forms new aerosol particles in marine environments. ENVIRON developed a chemical mechanism for iodine and ozone based on recent studies (Sommariva et al, 2012; Ordonez et al., 2012; Mahajan et al., 2010) and an emission model for oceanic emissions of iodine compounds for use with CAMx (Ordonez et al., 2012).

The iodine-ozone mechanism was integrated with CB6 in CAMx and tested using the Rider 8 modeling database developed by TCEQ for June 2006. CAMx sensitivity tests indicate that iodine chemistry may cause up to about 5 ppb of ozone depletion over the Gulf of Mexico and at coastal monitors in Texas. These estimates are uncertain because emissions of iodine-containing compounds are uncertain and no measurements are available in Texas for model evaluation. The iodine-ozone chemistry mechanism also is uncertain, but benefits from being based on studies (Sommariva et al, 2012; Ordonez et al., 2012; Mahajan et al., 2010) that have tested chemical mechanisms against detailed atmospheric measurements.

Analyses of detailed field study measurements for iodine and bromine at the Cape Verde Islands in the tropical Atlantic Ocean (Mahajan et al., 2010) have shown that bromine reactions cause ozone depletion comparable to iodine, and that iodine and bromine act synergistically. Accordingly, we recommend extending the emissions and chemistry algorithms developed here for iodine to also include bromine. We also recommend that global models used to develop ozone boundary conditions for TCEQ's CAMx modeling also should include reactions and oceanic emissions for include bromine.

5.0 REFERENCES

Atkinson, R.A., D.L. Baulch, R.A. Cox, J.N. Crowley, R.F. Hampson, R.G. Hynes, M.E. Jenkin, J.A. Kerr, M.J. Rossi, and J. Troe. 2010. "Evaluated kinetic and photochemical data for atmospheric chemistry - IUPAC subcommittee on gas kinetic data evaluation for atmospheric chemistry." 3 January 2010 web version available from http://www.iupac-kinetic.ch.cam.ac.uk/index.html

Bell, N., L. Hsu, D.J. Jacob, M.G. Schultz, D.R. Blake, J.H. Butler, D.B. King, J.M. Lobert, and E. Maier-Reimer. 2002. Global budgets of oceanic and atmospheric methyl iodide: development of methyl iodide as a tracer for marine convection in atmospheric models, *J. Geophys. Res.*, 107(D17), doi:10.1029/2011JD001151.

Bey, I., D. J. Jacob, R. M. Yantosca, J. A. Logan, B. D. Field, A. M. Fiore, Q. Li, H. Y. Liu, L. J. Mickley, and M. G. Schultz. 2001. Global modeling of tropospheric chemistry with assimilated meteorology: Model description and evaluation, Journal of Geophysical Research, 106, 23,073–23,096.

Carpenter, L.J. 2003. Iodine in the marine boundary layer. Chemical Reviews 103, 4953-4962.

Chambers, R. M., A. C. Heard, and R. P. Wayne. 1992. Inorganic gas-phase reactions of the nitrate radical: iodine + nitrate radical and iodine atom + nitrate radical. J. Phys. Chem., 96, 3321–3331. DOI: 10.1021/j100187a028

Chameides, W. L., and D. D. Davis. 1980. Iodine: Its Possible Role in Tropospheric Photochemistry, *J. Geophys. Res.*, 85, 7383–7398, doi:10.1029/JC085iC12p07383.

Cotter E.S.N., N.J. Booth, and C.E. Canosa-Mas, R.P. Wayne. 2001. Release of iodine in the atmospheric oxidation of alkyl iodides and the fates of iodinated alkoxy radicals, *Atmospheric Environment*, 35, 2169–2178

Dillon, T.J., M.E. Tucceri, and J.N. Crowley. 2006. Laser induced fluorescence studies of iodine oxide chemistry. Part II: the reactions of IO with CH3O2, CF3O2 and O3. Physical Chemistry Chemical Physics 8, 5185–5198.

Dillon, T.J., M.E. Tucceri, and J.N. Crowley. 2010. Rate coefficients for the reaction of iodine oxide with methyl peroxy radicals. ChemPhysChem 11, 4011-4018.

Emmons, L. K., S. Walters, P. G Hess, J.-F Lamarque, G. G. Pfister, D. Fillmore, C. Granier, A. Guenther, D. Kinnison, T. Laepple, J. Orlando, X. Tie, G. Tyndall, C. Wiedinmyer, S. L. Baughcum, and S. Kloster. 2010. Description and evaluation of the Model for Ozone and Related chemical Tracers, version 4 (MOZART-4), Geosci. Model Dev., 3, 43-67, doi:10.5194/gmd-3-43-2010.

ENVIRON. 2012. "User's Guide: Comprehensive Air quality Model with extensions, Version 5.40." Prepared by ENVIRON International Corporation. Available from http://www.camx.com.

Fiore, A. M., et al. 2009. Multimodel estimates of intercontinental source-receptor relationships for ozone pollution, J. Geophys. Res., 114, D04301, doi:10.1029/2008JD010816.

Folberth, G. A., D.A. Hauglustaine, J. Lathière, and F. Brocheton. 2006. Interactive chemistry in the Laboratoire de Météorologie Dynamique general circulation model: model description and impact analysis of biogenic hydrocarbons on tropospheric chemistry, Atmos. Chem. Phys., 6, 2273-2319, doi:10.5194/acp-6-2273-2006.

Ganzeveld, L., D. Helmig, C. W. Fairall, J. Hare, and A. Pozzer. 2009. Atmosphere-ocean ozone exchange: A global modeling study of biogeochemical, atmospheric, and waterside turbulence dependencies, Global Biogeochem. Cycles, 23, GB4021, doi:10.1029/2008GB003301.

Gómez-Martín, J.C., P. Spietz, and J.P. Burrows. 2007. Kinetic and mechanistic studies of the I2/O3 photochemistry. Journal of Physical Chemistry A 111, 306–320.

Helmig, D., E.K. Lang, L. Bariteau, P. Boylan, C.W. Fairall, L. Ganzeveld, J.E. Hare, and J. Hueber, M. Pallandt. 2012. "Atmospherie-ocean ozone fluxes during the TexAQS 2006, STRATUS 2006, GOMECC 2007, GasEx 2008 and AMMA 2008 Cruises." *J. Geophys. Res.*, 117, D04305, doi:10.1029/2011JD015955.

HTAP 2007. Hemispheric Transport of Air Pollutants 2007: An Interim Report of the Task Force on Hemispheric Transport of Air Pollutants of the Convention on Long-range Transboundary Air Pollution (Draft, August). Available at http://www.htap.org/assessment/2007_interim_report/TF%20HTAP%202007%20070831.pdf accessed 22 August 2012.

Joseph, D.M., S.H. Ashworth and J.M.C. Plane. 2005. The absorption cross-section and photochemistry of OIO. Journal of Photochemistry and Photobiology A – Chemistry 176, 68–77.

Kaltsoyannis, N., Plane, and J.M.C. 2008. Quantum chemical calculations on a selection of iodine-containing species (IO, OIO, INO3, IO2, I2O3, I2O4 and I2O5) of importance in the atmosphere. Physical Chemistry Chemical Physics 10, 1723–1733.

Mahajan, A. S., J.M.C., Plane, H. Oetjen, L Mendes, R.W. Saunders, A. Saiz-Lopez, C.E. Jones, L.J. Carpenter, and G.B. McFiggans. 2010. Measurement and modelling of tropospheric reactive halogen species over the tropical Atlantic Ocean, Atmos. Chem. Phys., 10, 4611-4624, doi:10.5194/acp-10-4611-2010.

Moore, R. and Tokarczyk, R. 1993. Volatile Biogenic Halocarbons in the Northwest Atlantic, Global Biogeochem. Cy., 7, 195–210,

Moore, R. and Zafiriou, O. 1994. Photochemical production of methyl iodide in seawater, J. Geophys. Res., 99, 16415–16420, doi:10.1029/94JD00786.

Ordóñez, C., J.-F. Lamarque, S. Tilmes, D.E. Kinnison, E.L. Atlas, D.R. Blake, G. Sousa Santos, G. Brasseur, and A. Saiz-Lopez. 2012. Bromine and iodine chemistry in a global chemistry-

climate model: description and evaluation of very short-lived oceanic sources, Atmos. Chem. Phys., 12, 1423-1447, doi:10.5194/acp-12-1423-2012.

Plane, J.M.C., Joseph, D.M., Allan, B.J., Ashworth, S.H., and Francisco, J.S. 2006. An experimental and theoretical study of the reactions OIO + NO and OIO + OH. Journal of Physical Chemistry 110, 93–100.

Reidmiller, D. R., A.M. Fiore, D.A. Jaffe, D. Bergmann, C. Cuvelier, F. J. Dentener, B.N. Duncan, G. Folberth, M. Gauss, S. Gong, P. Hess, J.E. Jonson, T. Keating, A. Lupu, E. Marmer, R. Park, M.G. Schultz, D. T. Shindell, S. Szopa, M.G. Vivanco, O. Wild, and A. Zuber. 2009. The influence of foreign vs. North American emissions on surface ozone in the US, Atmos. Chem. Phys., 9, 5027-5042, doi:10.5194/acp-9-5027-2009.

Riffault, V., Y. Bedjanian, and G. Poulet. 2005. Kinetic and mechanistic study of the reactions of OH with IBr and HOI. Journal of Photochemistry and Photobiology A – Chemistry, 176, 155–161.

Saiz-Lopez, A. and Plane, J. M. C. 2004. Novel iodine chemistry in the marine boundary layer, Geophys. Res. Lett., 31, L04112, doi:10.1029/2003GL019215.

Sander, S.P., R.R. Friedl, D. M. Golden, M. J. Kurylo, G. K. Moortgat, P. H. Wine, A. R. Ravishankara, C. E. Kolb, M. J. Molina, B. J Finlayson-Pitts, R. E. Huie, and V. L. Orkin. 2006. "Chemical Kinetics and Photochemical Data for use in Atmospheric Studies, Evaluation Number 15. NASA Jet Propulsion Laboratory." July. Available from http://jpldataeval.jpl.nasa.gov/download.html.

Saunders, R.W., and J.M.C. Plane. 2005. Formation pathways and composition of iodine oxide ultra-fine particles. Environmental Chemistry 2, 299–303.

Sehmel, G.A. 1980. "Particle and Gas Deposition, a Review." *Atmos. Environ.*, 14, 983-1011.

Sommariva R., W.J. Bloss, and R. von Glasow. 2012. Uncertainties in gas-phase atmospheric iodine chemistry, Atmospheric Environment , 57 219–232. doi:10.1016/j.atmosenv.2012.04.032.

Tai E., B. Koo, P. Piyachaturawat and G. Yarwood. 2009. Updated Boundary Conditions. Report prepared by ENVIRON for TCEQ Work Order No. 582-07-84005-FY09-16.

TCEQ 2012. Rider 8 State and Local Air Quality Planning Program - Modeling Domains. Available at http://www.tceq.texas.gov/airquality/airmod/rider8/modeling/domain, accessed 22 August 2012.

van den Bergh, H. and Troe, J. 1976. Kinetic and thermodynamic properties of INO and INO_2 intermediate complexes in iodine recombination. J. Chem. Phys., 64, 736–742.

Wesely, M.L. 1989. "Parameterization of Surface Resistances to Gaseous Dry Deposition in Regional-Scale Numerical Models." *Atmos. Environ.*, 23, 1293-1304.

Zhang, L., J.R. Brook, and R. Vet. 2003. "A revised parameterization for gaseous dry deposition in air-quality models." *Atmos. Chem. Phys.*, 3, 2067–2082.